



Three Eruptions Observed by Remote Sensing Instruments Onboard Solar Orbiter

Marilena Mierla^{1,2} · Hebe Cremades³ · Vincenzo Andretta⁴ · Iulia Chifu⁵ · Andrei N. Zhukov^{1,6} · Roberto Susino⁷ · Frédéric Auchère⁸ · Angelos Vourlidas⁹ · Dana-Camelia Talpeanu¹ · Luciano Rodriguez¹ · Jan Janssens¹ · Bogdan Nicula¹ · Regina Aznar Cuadrado¹⁰ · David Berghmans¹ · Alessandro Bemporad⁷ · Elke D’Huys¹ · Laurent Dolla¹ · Samuel Gissot¹ · Giovanna Jerse¹¹ · Emil Kraaikamp¹ · David M. Long^{12,13} · Benjamin Mampaey¹ · Christian Möstl¹⁴ · Paolo Pagano^{15,16} · Susanna Parenti⁸ · Matthew J. West¹⁷ · Olena Podladchikova^{18,19} · Marco Romoli^{20,21} · Clementina Sasso⁴ · Koen Stegen¹ · Luca Teriaca¹⁰ · William Thompson²² · Cis Verbeek¹ · Emma Davies²³

Received: 22 November 2022 / Accepted: 21 February 2023
© The Author(s) 2023

Abstract

On February 21 and March 21–22, 2021, the Extreme Ultraviolet Imager (EUI) onboard Solar Orbiter observed three prominence eruptions. The eruptions were associated with coronal mass ejections (CMEs) observed by Metis, Solar Orbiter’s coronagraph. All three eruptions were also observed by instruments onboard the Solar–Terrestrial Relations Observatory (Ahead; STEREO-A), the Solar Dynamics Observatory (SDO), and the Solar and Heliospheric Observatory (SOHO). Here we present an analysis of these eruptions. We investigate their morphology, direction of propagation, and 3D properties. We demonstrate the success of applying two 3D reconstruction methods to three CMEs and their corresponding prominences observed from three perspectives and different distances from the Sun. This allows us to analyze the evolution of the events, from the erupting prominences low in the corona to the corresponding CMEs high in the corona. We also study the changes in the global magnetic field before and after the eruptions and the magnetic field configuration at the site of the eruptions using magnetic field extrapolation methods. This work highlights the importance of multi-perspective observations in studying the morphology of the erupting prominences, their source regions, and associated CMEs. The upcoming Solar Orbiter observations from higher latitudes will help to constrain this kind of study better.

Keywords Coronal mass ejections · Low coronal signatures · Coronal mass ejections · Initiation and propagation · Prominences · Dynamics

1. Introduction

Coronal mass ejections (CMEs) are the most energetic transient phenomena in the solar atmosphere. During CMEs, magnetized solar plasma is ejected from the Sun at velocities

Extended author information available on the last page of the article

ranging from less than 200 km s^{-1} to more than 2000 km s^{-1} (Hundhausen, Burkepile, and St. Cyr, 1994; Dryer et al., 2012; Liou et al., 2014). CMEs are observed as having a very large variety of apparent morphologies from loop-like shapes to more complex structures like ‘three-part’ CMEs (Illing and Hundhausen, 1986), where the bright front is followed by a darker cavity, which frequently contains a bright, compact core. CMEs are highly dynamic events whose global appearance may change considerably in successive images. Even though CMEs are observed mostly in visible light (VL) images by means of coronagraphs, their origins are rooted deeper in the solar atmosphere, see, e.g., the review of CMEs by Webb and Howard (2012).

Extreme ultraviolet (EUV) imagers and VL coronagraphs onboard NASA’s Solar–TERrestrial RELations Observatory (STEREO: Kaiser et al., 2008), ESA’s PROject for On Board Autonomy 2 (PROBA2: Santandrea et al., 2013) and NASA’s Solar Dynamics Observatory (SDO: Pesnell, Thompson, and Chamberlin, 2012) space missions have observed the Sun almost continuously and simultaneously for the last 12 years. They have provided complementary data to those from the joint ESA–NASA’s Solar and Heliospheric Observatory (SOHO: Domingo, Fleck, and Poland, 1995), on CMEs, their initiation, and associated phenomena such as prominences, observing the solar atmosphere from widely separated vantage points, with high spatial and temporal resolution and with good coverage of coronal heights. Having observations from more than one viewpoint enables a better understanding of the projection of a three-dimensional (3D) structure in two-dimensional (2D) space, leading to a more accurate determination of the CME speed and direction of propagation (see, e.g., Mierla et al., 2010). Furthermore, observations from multiple perspectives are the key ingredient needed to produce three-dimensional (3D) reconstructions (see, e.g., Thernisien, Vourlidas, and Howard, 2011).

The Full Sun Imager (FSI), a telescope of the Extreme Ultraviolet Imager (EUI) instrument (Rochus et al., 2020) onboard the ESA–NASA Solar Orbiter mission (Müller et al., 2020), added an extra viewpoint with images from its 174 \AA (FSI 174 \AA) and 304 \AA (FSI 304 \AA) channels. A particularly useful aspect of FSI for eruption studies is the large field of view (FOV) of 3.8 degrees, which provides a good overlap with the Metis FOV (Auchère et al., 2020). The Metis coronagraph (Antonucci et al., 2020) onboard Solar Orbiter is the first instrument observing both in polarised VL broad-band in the interval 580–640 nm, and in the UV narrow-band centered around the 121.6 nm Ly- α line emitted by neutral hydrogen (H) atoms (the most intense line in the UV solar spectrum). The large FOV of FSI also allows observations of the prominence eruptions to great heights never observed before by EUV imagers (Mierla et al., 2022). Prominences (or filaments, when they are seen projected on the solar disk) are cool and dense plasma structures observed in the hot and thin solar atmosphere (see, e.g., Gibson, 2018).

In this paper, the observations of three prominence eruptions acquired by the aforementioned remote sensing instruments onboard Solar Orbiter are analyzed (see Section 2). One eruption took place on February 21, 2021, and two others on March 21–22, 2021. They propagate in different directions with respect to the Earth, STEREO-A and Solar Orbiter. Two reconstruction methods, triangulation (Inhester, 2006) and graduated cylindrical shell (GCS) model (see, e.g., Thernisien, Vourlidas, and Howard, 2009; Thernisien, 2011), are applied in order to derive the 3D coordinates of the erupting prominences and of the corresponding CMEs, respectively (see Section 3). The GCS technique has already been applied successfully to case-studied CMEs observed by Metis (Andretta et al., 2021; Bemporad et al., 2022) and by the Wide-Field Imager for Solar PRobe (WISPR: Vourlidas et al., 2016) onboard the Parker Solar Probe (PSP: Fox et al., 2016) mission (Braga et al., 2021). Here, we further demonstrate the success of applying the GCS and triangulation methods to three

CMEs and their associated prominences seen from three different viewing angles and distances to the Sun (see Sections 3 and 5). This allowed us to study the deflections of the erupting events while propagating from lower to higher altitudes in the corona. We have also applied the Potential Field Source Surface (PFSS) (Altschuler and Newkirk, 1969; Wang and Sheeley, 1992; Schrijver and De Rosa, 2003) extrapolation method for obtaining the global magnetic field configuration before and after the eruptions as well as the nonlinear force-free field (NLFFF) (Wheatland, Sturrock, and Roumeliotis, 2000; Wiegelmann, 2004; Wiegelmann and Inhester, 2010; Tadesse et al., 2011) extrapolation method in order to obtain the magnetic-field configuration at the site of the eruptive prominences (see Section 4).

2. Observations

Three prominence eruptions were observed by FSI 304 Å on February 21 and March 21 – 22, 2021 (see Figure 1). Other EUV telescopes that observed the eruptions and were used in this study were EUVI (Howard et al., 2008) onboard the STEREO-A spacecraft, and AIA (Lemen et al., 2012) onboard SDO.

The selection criteria for these events were based on the fact that they were among the first eruptions observed by both EUI and Metis instruments that had acceptable cadence. They were observed from different distances from the Sun and different perspectives (STEREO-A, Solar Orbiter, and Earth). Another selection criterion was having different views from the three perspectives, such that the prominences were observed on-disk in at least one view. Such different views (on-disk and off-limb) helped us disentangle their morphology better.

The first eruption (hereafter *Eruption 1*) started at around 00:00 UT on February 21 to the North-West (NW) of the Sun as seen from FSI. The other two eruptions were observed on March 21, one starting around 11:00 UT to the NW, and one around 20:00 UT to the South-West (SW) of the Sun (hereafter *Eruption 2* and *Eruption 3*, respectively). Both prominences are still visible on March 22.

The corresponding CMEs were subsequently observed in VL by the Metis coronagraph onboard Solar Orbiter, by the COR1 and COR2 coronagraphs (Howard et al., 2008) onboard STEREO-A, and by the Large-Angle Spectroscopic CORonagraph (LASCO, Brueckner et al., 1995) onboard SOHO.

The positions of the different spacecrafts are shown in Figure 2 and Table 1.

Note that all on-disk position values in this study are given in Stonyhurst heliographic coordinates, unless it is stated otherwise. In the Stonyhurst coordinate system (Thompson, 2006), the origin is set at the intersection of the Sun's equator with the central meridian, as seen from the Earth. The time (in Universal Time - UT) represents the time when different instruments recorded the eruptions.

2.1. Eruption 1

Eruption 1 was observed by FSI 304 Å at its NW limb on February 21, 2021, starting at around 00:00 UT (see top-left panel of Figure 1). It was an elongated filament that spanned around 30 degrees in longitude and was slowly erupting as the FSI movie indicates. One extremity (*Ext1*) of the eruptive prominence is seen as bright material moving out at the NW limb of the FSI 304 Å image, indicated by the arrow in the top-left panel of Figure 1. The other extremity (*Ext2*) is seen on-disk (from the FSI perspective) as dark material expanding towards the central meridian. The erupting prominence is visible in the FSI 304 Å FOV until

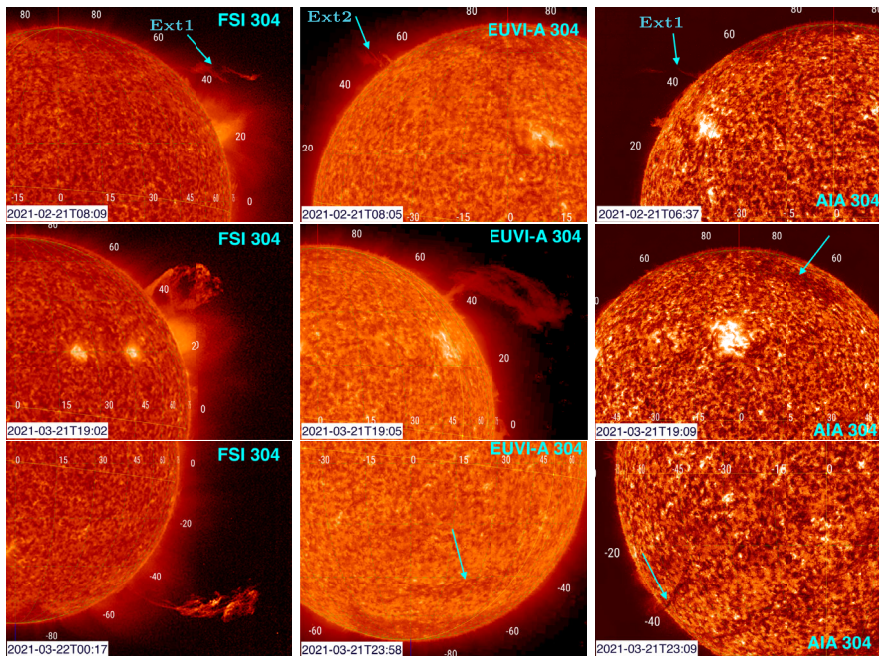


Figure 1 Eruptions observed by EUV 304 Å instruments. The *top* row corresponds to *Eruption 1* (and its composite parts, *Ext1* and *Ext2*), the *middle* row to *Eruption 2*, and the *bottom* row to *Eruption 3*. The first column consists of observations taken by FSI 304 Å, the second by EUVI-A 304 Å, and the third by AIA 304 Å. Animations of this figure are available as Electronic Supplementary Material. The FSI data are recorded during the commissioning phase, so the data quality is different from image to image.

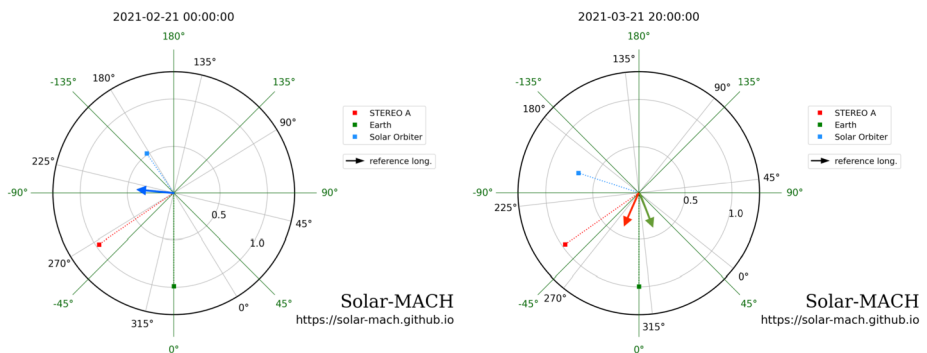


Figure 2 Positions of observing spacecraft on February 21 (*left panel*) and March 21 (*right panel*), 2021 in Carrington (*black*) and Stonyhurst (*green*) coordinate systems. The three arrows represent the propagation direction of the three eruptions (*blue, green, and red arrows for Eruption 1, Eruption 2, and Eruption 3, respectively*) as derived from the GCS reconstruction. The images were created using Solar-MACH (solar-mach.github.io/).

11:24 UT. The event was also observed by FSI 174 Å as a diffuse non-radial eruption, visible from around 07:00 UT to around 11:20 UT on February 21.

Table 1 Vantage points of the observations on February 21, 00:00 UT, and on March 21, 20:00 UT, 2021. The first column indicates the date and time in the format yyyy-mm-dd hh:mm. The second column shows the vantage point of the observations. The third column indicates the distance to the Sun in astronomical units, and the fourth column shows the latitude and longitude in degrees. The latitude and longitude are given in the Heliocentric Earth Equatorial (HEEQ) coordinate system (Thompson, 2006).

Date/Time UT	Vantage Point	Distance to the Sun [AU]	Latitude/Longitude [deg]
2021-02-21 00:00	Earth	0.988	S07E00
	STEREO-A	0.966	S03E56
	Solar Orbiter	0.515	N02E145
2021-03-21 20:00	Earth	0.996	S07E00
	STEREO-A	0.967	S06E55
	Solar Orbiter	0.687	N01E108

EUVI-A 304 Å observed a prominence eruption at its NE limb starting at around 05:30 UT (top-middle panel of Figure 1), which was visible until around 10:35 UT. As STEREO-A was in quadrature with Solar Orbiter at this time, *Ext1* of the filament should be seen on-disk, and *Ext2* should be seen off-limb (NE), from the perspective of STEREO-A. After a careful inspection of the EUVI-A 304 Å images, we indeed observe a faint dark filament structure (*Ext1*) slowly erupting on-disk. *Ext2* is clearly visible as a prominence eruption at the NE limb, which can be seen in the top-middle panel of Figure 1.

AIA 304 Å observed a prominence slowly erupting at the NE limb starting around 05:00 UT on February 21 (top-right panel of Figure 1). The prominence is visible in AIA FOV from 20:30 UT on February 21 to around 08:00 UT on February 21. As SDO was almost in opposition with Solar Orbiter, the *Ext2* of the prominence is an event behind the limb for AIA, but the top of the erupting arcade can still be briefly seen off-limb. The appearance of *Ext1* is similar in the AIA and FSI observations. AIA 171 Å observed an eruption at the NE limb from around 05:00 UT onwards.

As seen from the top panels of Figure 1, the visual appearance of the prominence in EUVI-A 304 Å image is different from the one in FSI 304 Å and AIA 304 Å confirming the different viewing perspectives.

Figure 3 shows the dimming observed in EUVI-A 195 Å at around 10:00 UT on February 21, from where a leg of this prominence most probably originated (red arrow). It is located at around N40E70. The location of *Eruption 1* was calculated by taking the position of this dimming and by adding a longitudinal extent of 30 degrees (based on the size of the prominence measured on-disk in FSI 304 Å image at around 08:00 UT on February 21) (see Table 2).

On the same day, Metis was running a program in the context of the second Solar Orbiter Remote-Sensing Check-out Window (February 20–25, 2021). Both VL and UV channels were operating. Here we show the results from the VL channel only. During these observations, a CME entered the NW sector of the Metis FOV at around 11:00 UT on February 21 (upper row of Figure 4). Its three-part configuration suggests that it is most probably associated with *Eruption 1*.

Eruption 1 was observed on February 21 by LASCO-C2 and by COR2-A as a slow three-part CME at the NE limb starting at around 08:00 UT (upper-right panel of Figure 5) and at the East limb, starting at around 11:30 UT (upper-left panel of Figure 5), respectively.

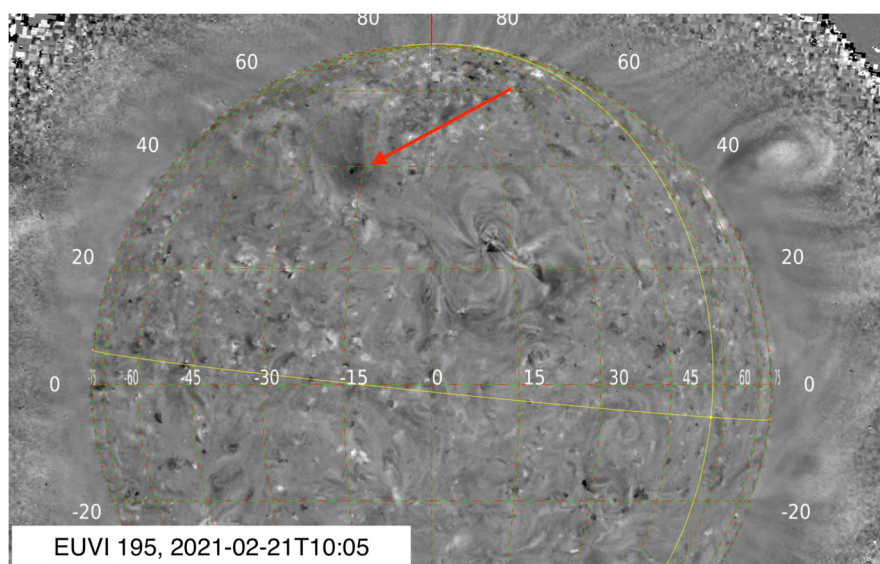


Figure 3 EUVI-A 195 Å base-difference image at 10:05 UT–04:05 UT showing the dimming from where one leg of the *Eruption 1* most probably originated.

Table 2 Latitudinal and longitudinal extent of the three prominences in the HEEQ coordinate system. The times for *Eruption 2* and *Eruption 3* represent the times when the location of the two prominences were identified in the AIA 304 Å and EUVI-A 304 Å images, respectively. The time for *Eruption 1* is when the dimming was observed in the EUVI-A 195 Å image. The size of *Eruption 1* was calculated by taking the position of one leg from the dimming observed in EUVI-A 195 Å at around 10:00 UT on February 21 and by adding a longitudinal extent of 30 degrees (based on the size of the prominence measured on-disk in FSI 304 Å image at around 08:00 UT on February 21).

Name	Date [yyyy-mm-dd]	Time [UT]	Latitude/Longitude [deg]
<i>Eruption 1</i>	2021-02-21	10:00	N40E75–N50E105
<i>Eruption 2</i>	2021-03-21	10:00	N40E02–N40W33
<i>Eruption 3</i>	2021-03-21	22:00	S40E55–S35E30

The speed of the CME as provided by the manual LASCO catalogue¹ (Yashiro et al., 2004) increased from around 75 km s^{-1} at 2.4 Rs to around 500 km s^{-1} at 28 Rs.

A more detailed description of *Eruption 1* and its observations can be found in Appendix A.

2.2. Eruption 2

Eruption 2 was observed by FSI 304 Å at the NW limb as a prominence slowly rising at around 11:00 UT on March 21, 2021, with a clear eruption visible from around 16:00 UT until 22:30 UT (see middle-left panel of Figure 1). After that time, the prominence looks stationary. Material falling back to the Sun is observed starting at around 21:00 UT. The

¹cdaw.gsfc.nasa.gov/CME_list/UNIVERSAL/2021_02/htpng/20210221.082406.p090g.htm.

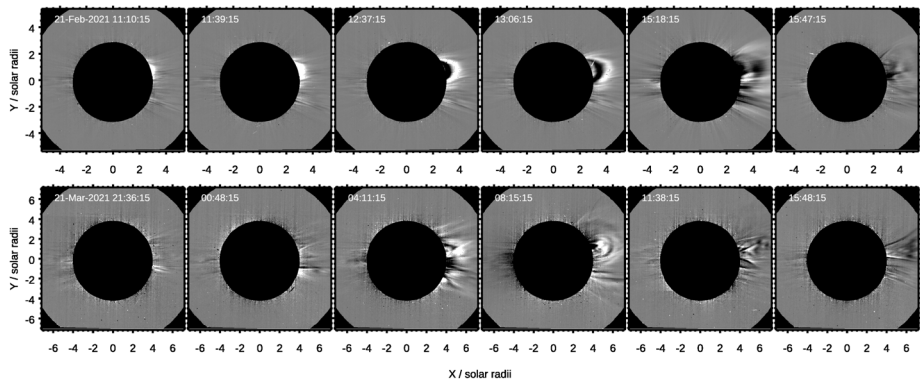


Figure 4 Running difference images of the CMEs observed by Metis on February 21 (*top row*) and March 22 (*bottom row*). In both cases, only a subset of images is shown. The cadence of these observations was of 30 minutes. An animation of this figure is available online.

prominence is seen until around 04:00 UT on March 22. The eruption was also observed by FSI 174 Å as slowly rising diffuse material at around 15:00 UT on March 21. Material is still seen moving outwards at around 00:00 UT on March 22.

Another (faster) eruption (which is not studied here because it did not have any associated prominence) was observed by FSI 174 Å and FSI 304 Å, around 15 degrees southern of *Eruption 2* starting before 01:00 UT on March 22. This faster eruption was associated with an on-disk origin located in active region NOAA 12810, at N30W00 Stonyhurst coordinates, as the dimming in SDO/AIA observations indicates. In AIA 304 Å this is observed as a white plage (see the middle-right panel of Figure 1).

AIA 304 Å observed a big filament on-disk in the Northern hemisphere (middle-right panel of Figure 1) starting to erupt at around 11:00 UT on March 21. The location of the filament as measured in AIA 304 Å image at 10:00 UT spans from N40E02 to N40W33 (see Table 2). After around 19:00 UT the erupting filament split in two, one part going towards NE and one part towards W-NW. From the observations, we believe that the two parts have a common leg. We identified the material erupting towards W-NW as being the *Eruption 2* studied here.

EUVI-A 304 Å observed *Eruption 2* as a big prominence slowly erupting at its NW limb, starting at around 01:15 UT on March 21. The prominence was visible off-limb already at 22:00 UT on March 20. At 22:30 UT on March 21, the erupting material remains visible in the EUVI-A 304 Å FOV. The base of the prominence is seen until around 01:00 UT on March 22.

Metis detected in its VL channel a flux-rope-like CME starting from about 03:00 UT on March 22 (lower row of Figure 4). This CME followed another fainter event, visible in the online movie around 02:00 UT or later, and most probably related to the dimming observed by AIA at around 01:00 UT in NOAA 12810. The structured CME is associated with *Eruption 2*.

LASCO-C2 and COR2-A observed a structured CME to the NW, starting at the end of the day on March 21 (lower panels of Figure 5), most probably associated with *Eruption 2*. The speed of the CME as provided by the manual LASCO catalogue² decreased from around

²cdaw.gsfc.nasa.gov/CME_list/UNIVERSAL/2021_03/htpng/20210322.021206.p304g.htm.

230 km s⁻¹ at 2.8 Rs to around 150 km s⁻¹ at 7 Rs. A diffuse partial-halo CME overtaking this CME is observed by LASCO-C2 starting at around 05:00 UT–06:00 UT on March 22. This CME is most probably associated with the dimming observed by AIA at around 01:00 UT (N30W00) and not studied in this work. COR2-A observed diffuse outflows to the NW starting early on March 21 and throughout the rest of the day.

More details on *Eruption 2* and its observations can be found in Appendix A.

2.3. Eruption 3

Eruption 3 was observed by FSI 304 Å on March 21, 2021, starting at around 20:00 UT at the SW limb (see lower-left panel of Figure 1). The erupting material is seen rising until around 03:00 UT on March 22. The eruption is also observed by FSI 174 Å starting around 21:00 UT on March 21 and last seen around 01:00 UT on March 22.

AIA 304 Å observed *Eruption 3* as a filament on-disk, close to the SE limb starting to erupt at around 21:00 UT–22:00 UT on March 21 (see lower-right panel of Figure 1). The last frame showing the eruption is around 00:10 UT on March 22.

EUVI-A 304 Å observed the same event as a big filament erupting from the disk at around 21:00 UT–22:00 UT, in the Southern hemisphere (see lower-middle panel of Figure 1). The location of the filament as measured in EUVI-A 304 Å image at 22:00 UT is from S40E55 to S35E30 (see Table 2). During the eruption, we observe that the right leg is disconnected first, and the erupting material is going towards SE. The last frame when the eruption is still visible is at around 03:00 UT on March 22.

Eruption 3 is detected by Metis in its VL channel as a faint and narrow CME to the SW starting around 01:17 UT on March 22. It becomes wider around 03:00 UT–04:00 UT. After that time, its northern flank seems to merge with the much brighter *Eruption 2* and becomes fainter. Another elongated blob-like CME was observed by Metis earlier, coming from the same position off-limb on March 21 at around 21:30 UT.

LASCO-C2 observed *Eruption 3* as a structured CME to the SE, starting at around 02:00 UT on March 22 (lower-right panel of Figure 5). The speed of the CME as provided by the manual LASCO catalogue³ increased from around 250 km s⁻¹ at 2.5 Rs to around 350 km s⁻¹ at 13 Rs.

A very faint CME is visible in COR2 base-difference images to the SE at around 04:00 UT–06:00 UT on March 22. This CME is most probably associated with *Eruption 3*.

A more detailed explanations of the observations and the instrumental characteristics are given in Appendix A.

3. 3D Reconstruction

3.1. Triangulation

The triangulation method requires identification of the same point in two images (Image 1 and Image 2) taken from different perspectives, a process called tie-pointing (see, e.g., Inhester, 2006). We determine the 3D positions of lines of sight (LOS) passing through the point that is visible in the two images, and we determine the position of the intersection point in 3D space.

³cdaw.gsfc.nasa.gov/CME_list/UNIVERSAL/2021_03/htpng/20210322.002406.p108g.htp.html.

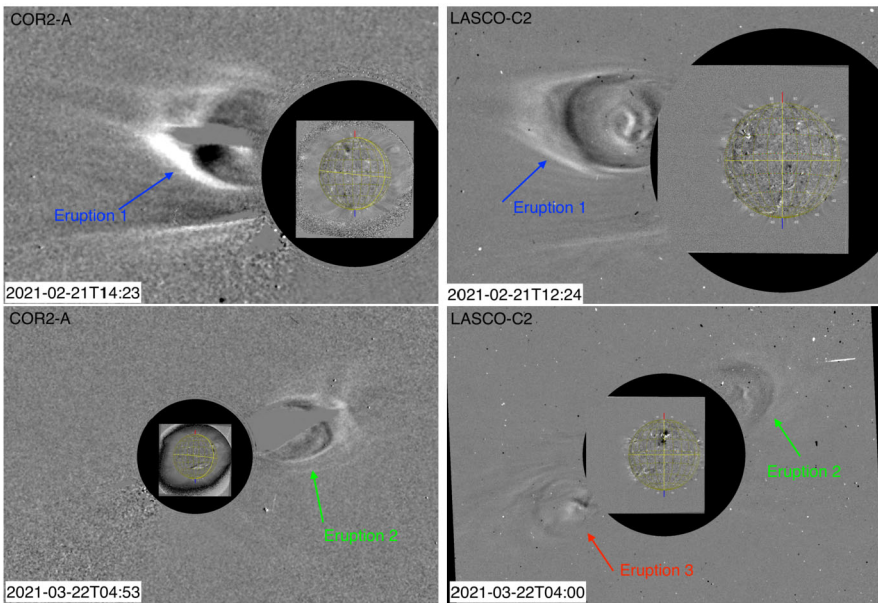


Figure 5 COR2-A (left panels) and LASCO-C2 (right panels) running-difference images showing the CMEs on February 21 (upper panels) and March 22 (lower panels). Base-difference SWAP (12:25 UT – 00:00 UT on February 21 and 03:59 UT – 00:01 UT on March 22) and EUVI-A 195 Å (14:27 UT – 00:05 UT on February 21 and 04:52 UT – 00:10 UT on March 22) images are overlapped onto the observations taken by LASCO-C2 and COR2-A, respectively. The times represent those of the current image and of the base image that was subtracted, respectively.

The identification of the same feature in two images (i.e., two observations from two spacecraft located in different vantage points) is sometimes a complicated procedure if the feature projected on the images does not have the same shape. One simplification comes if we employ the epipolar geometry, i.e. if we look for the counterpart of the feature identified in Image 1 along its epipolar line in Image 2. The epipolar line is the projection of the LOS of the feature identified in one image on the second image (e.g., Inhester, 2006). Therefore, the search of the counterpart of the feature identified in Image 1 is not done in the entire Image 2 but just along a line.

We performed triangulation for the three prominences studied here using the `scc_measure.pro` program of SolarSoft (Thompson and Reginald, 2008; Thompson, 2009). The program allows us to manually select a point in our feature of interest in one image and draws its corresponding epipolar line in the second image. By selecting the corresponding feature along the epipolar line in the second image, the program outputs the position of the feature in Stonyhurst coordinates (longitude, latitude, and height from the Sun's center). As we were only interested in following the direction of propagation of the three prominences in time (and not its 3D morphology), we selected only one point that was easily identifiable in the outer part of each prominence (see Figure 6). The results of the triangulation applied to our eruptions are shown in Table 3.

The upper panel of Figure 6 shows the prominence observed by FSI 304 Å (left) and AIA 304 Å (right) on February 21 at around 07:40 UT. The epipolar line is approximately along the prominence main axis in the second image, but the same feature could be identified in the two images due to its similar shape (bulged part of the prominence, white crosses).

Table 3 3D parameters for the three prominences studied here, as derived from triangulation. *First column:* Date and time of the reconstruction in FSI. *Second column:* the latitude and longitude in Stonyhurst coordinates. *Third column:* height of the prominence measured from the Sun's center, in solar radii (Rs). *Fourth column:* instruments used for triangulation.

Date and time [yyyy – mm – dd hh : mm]	Latitude/Longitude [deg]	Height [Rs]	Instruments
2021-02-21 07:39	N37E97	1.33	FSI+AIA
2021-03-21 16:02	N29W17	1.36	FSI+EUVI-A
2021-03-22 00:02	S27E35	1.68	FSI+AIA

This feature was triangulated, resulting in a position of N37E97 and a height of around 1.33 Rs from the Sun's center.

For the two prominence eruptions observed on March 21 – 22, the identification of the same features was more difficult as the shape of the prominences in the corresponding images looked different (see middle and lower panels of Figure 6). The identification was made by selecting the outermost point of the prominence in one image and its corresponding point along the epipolar line in the second image.

3.2. GCS Reconstruction

We applied the GCS geometrical model in order to derive the 3D position and extent of each of the three CMEs higher in the corona (see Figure 7).

The GCS model is meant to reproduce the large-scale structure of flux rope-like CMEs. It consists of a tubular curved section forming the main body of the structure connected to two cones attached to the Sun that correspond to the “legs” of the CME. Only the surface of the CME is modeled, there is no rendering of its internal structure. This gives us information on the propagation of the leading edge of the CME. The model fits the geometrical structure of CMEs as observed by VL coronagraphs at different vantage points. The GCS reconstruction outputs are: the propagation longitude and latitude, the half-angular width (i.e., the half-angular distance between the leg axes), the aspect ratio (i.e., the ratio of the CME size at two orthogonal directions), the tilt angle with respect to the solar equator, and the leading-edge height of the CME.

To perform the reconstructions, for each event (*Eruption 1*, *Eruption 2*, *Eruption 3*), three images taken from three different perspectives (Metis on Solar Orbiter, COR2-A on STEREO-A and LASCO-C2 on SOHO) are used (see also Figure 2 and Table 1). LASCO-C2 and COR2-A were observing the CMEs from approximately 1 AU, while Metis was observing the CMEs from ≈ 0.5 AU (*Eruption 1*) and 0.7 AU (*Eruption 2*, *Eruption 3*). The separation angle between the Earth and STEREO-A was 55 degrees for all three eruptions. The separation angle between Solar Orbiter and STEREO-A was 90 degrees for *Eruption 1*, and 55 degrees for *Eruption 2* and *Eruption 3*. Reconstructions are done at the time with the least time difference between images from the three perspectives, with the CME leading edge still in the FOV of Metis while somewhat developed in COR2-A. Due to the different FOVs of the coronagraphs, the CME has already left the Metis FOV when it is well observed in COR2-A. Therefore, the time overlap between the three coronagraphs during which the events can be simultaneously observed is a few tens of minutes.

The resulting parameters of the GCS reconstruction are shown in Table 4, while the fitted GCS shapes are displayed as green meshes in Figure 7. The different propagation directions of the three eruptions with respect to the three spacecraft are also depicted in Figure 2. From

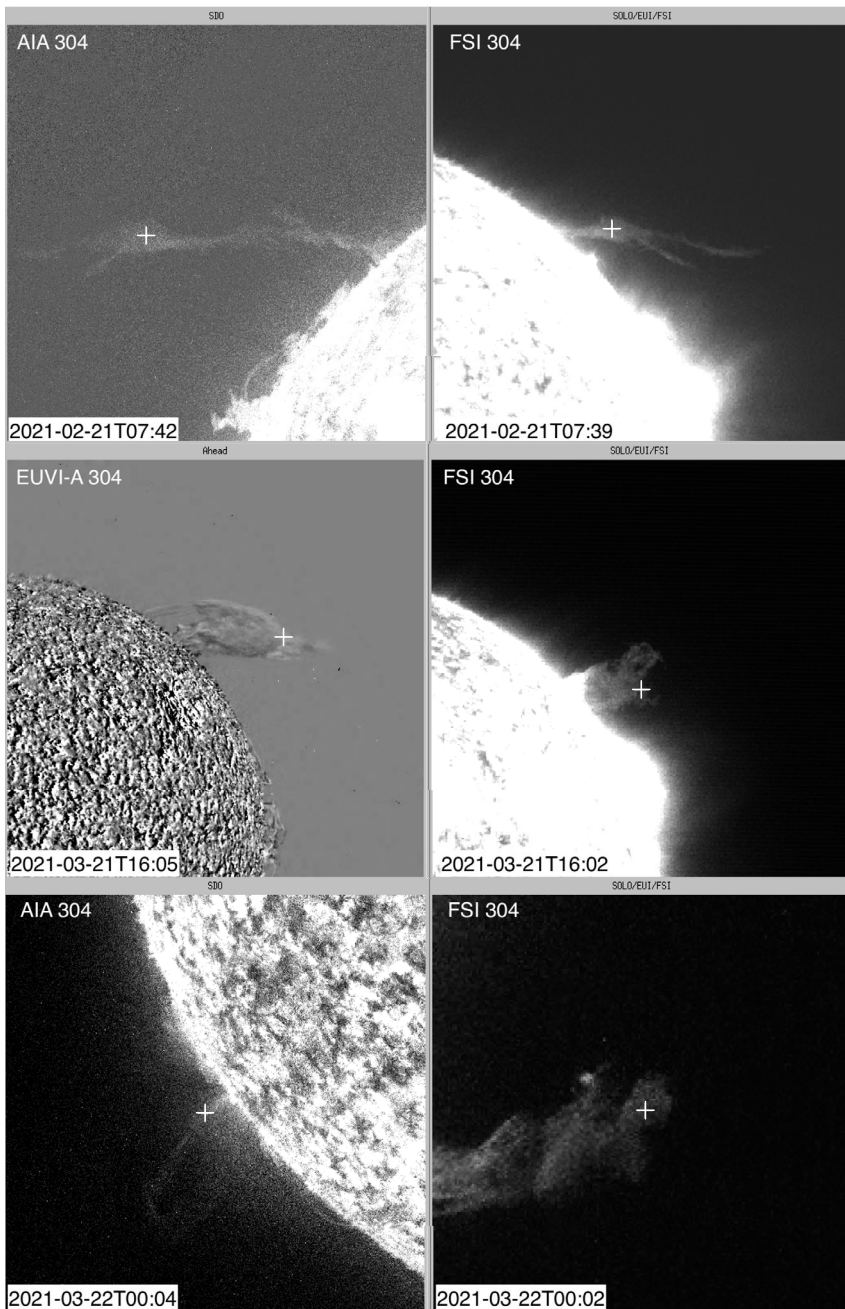


Figure 6 Prominence features chosen for triangulation. *Upper panels:* Triangulated feature (white crosses) performed with AIA 304 Å (left) and FSI 304 Å (right) on February 21 2021, 07:39 UT (*Eruption 1*). *Middle panels:* Triangulated feature of the prominence observed by FSI 304 Å (right) and EUVI-A 304 Å (left) on March 21, 16:02 UT (*Eruption 2*). *Lower panels:* Triangulated feature of the prominence observed by FSI 304 Å (right) and AIA 304 Å (left) on March 22, 00:02 UT (*Eruption 3*). The images are created with `scc_measure.pro`.

Table 4 3D CME parameters derived from the GCS fitting. *First column:* Date and time of the reconstruction in Metis. *Second column:* the latitude and longitude of the CME in Stonyhurst coordinates. *Third column:* Height of the CME front from the Sun's center. *Fourth column:* Tilt angle with respect to the solar equator. *Fifth and Sixth columns:* Aspect ratio and half angle of the CME, respectively.

CME Date and time [yyyy – mm – dd hh : mm]	Latitude/Longitude [deg]	Height [Rs]	Tilt angle [deg]	Ratio	Half angle [deg]
2021-02-21 13:21	N11E95	5.30	–5	0.30	15
2021-03-22 07:03	N16W23	8.20	40	0.23	12
2021-03-22 04:26	S23E25	8.90	10	0.25	20

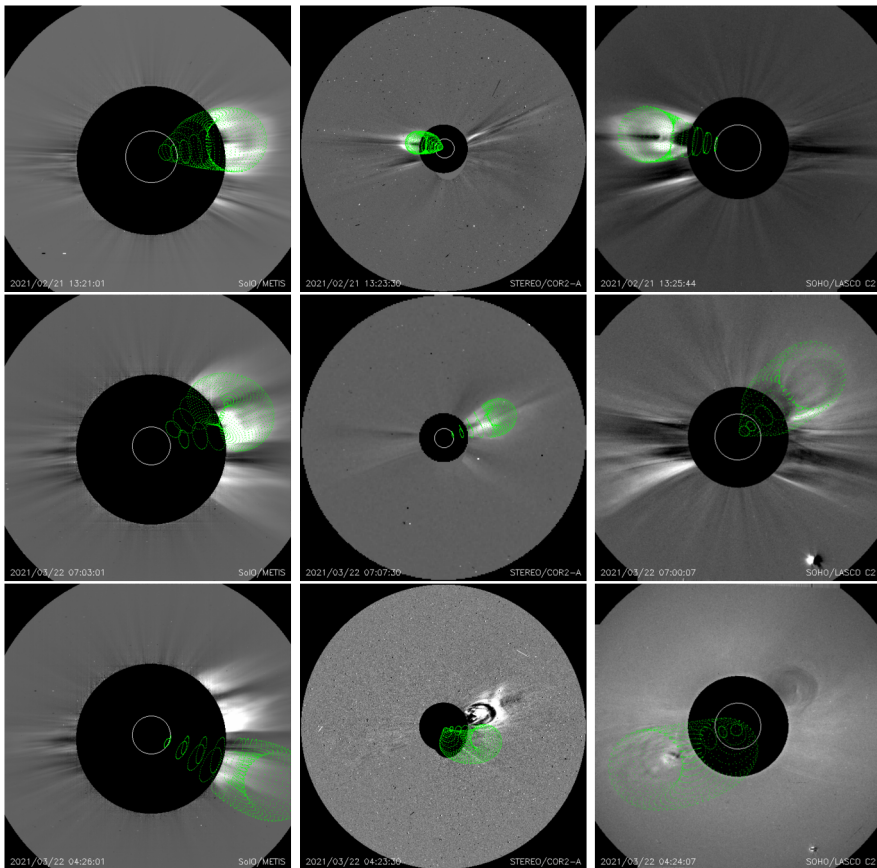


Figure 7 GCS reconstruction for *Eruption 1* (upper panels), *Eruption 2* (middle panels) and *Eruption 3* (lower panels) performed on Metis (left column), COR2-A (middle column) and LASCO-C2 (right column) observations. Note that *Eruption 3* is very faint in the COR2-A image (lower-middle panel), where the bright CME to the north of the *green mesh* corresponds to *Eruption 2*.

this, we can extract that *Eruption 1* was propagating between STEREO-A and Solar Orbiter, while *Eruption 2* was propagating mostly towards the Earth. *Eruption 3* was propagating between the Earth and STEREO-A.

4. Magnetic Field Analysis

In order to magnetically analyze the eruptions, we obtained the global as well as local magnetic field using two different extrapolation methods. We applied the potential field extrapolation method for acquiring the global magnetic field configuration before and after the three eruptions. We applied the NLFFF method to obtain the magnetic field configuration at the site of the eruptions. We only show the NLFFF results for *Eruption 2* as results for the other two cases did not reveal conclusive information because the magnetic field was more potential and did not show a helical topology. The lack of convincing results for *Eruptions 1* and *3* could be attributed to their location in regions of weak magnetic field far away from any active regions, whereas *Eruption 2* was closer to an active region with stronger magnetic field. NLFFF may give reliable results in or around active regions where the magnetic field is stronger.

For both magnetic field extrapolation methods, we used magnetic field data from the Helioseismic and Magnetic Imager (HMI: Schou et al., 2012) instrument onboard SDO. The magnetic field extrapolation techniques and the magnetic field data are described in detail in Appendix B.

In the following subsections, we present the results of the extrapolations.

4.1. Results of the PFSS

We show the results of the PFSS method related to the three prominence eruptions in order to assess the global magnetic field before and after the eruptions.

From the solution of the PFSS extrapolation for February 21 and March 21, we traced magnetic field lines in the corona. In Figure 8, we show a selection of the traced field lines overplotted on the synchronic map of Br (the building of the synchronic maps is described in Appendix B.1). The red loops have maximum heights of 1.5 Rs, the yellow field lines extend between 1.5 Rs and 2.0 Rs. We did not plot the field lines with heights between 2.0 Rs and 2.56 Rs. The blue ones are the field lines still open at 2.56 Rs. To identify changes in the magnetic field topology from February 21 to February 22 and from March 21 to March 22, we applied differential rotation to the footpoints of all selected loops on February 21 and March 21. The new footpoints are obtained using the differential rotation expression, $\Omega(\theta) = A + B \sin^2 \theta + C \sin^4 \theta$, where θ is the latitude, with the coefficients $A = 14.27$ degrees per day, $B = -1.46$ degrees per day, and $C = -2.66$ degrees per day (Hrazdírka, Druckmüller and Habbal, 2021). We used the new footpoints to trace the field lines from the solution of the PFSS extrapolation for February 22 (upper-right panel of Figure 8) and March 22 (bottom-right panel of Figure 8), respectively. Left panels of Figure 8 show a couple of traced loops before the prominences lifted off, and the right panels of Figure 8 show the field lines after the prominences erupted. From the topology, we can notice a strong change in the configuration of the magnetic field. We observe a depletion of the traced closed field lines from before and after the eruptions. Some of the closed magnetic field lines (red and yellow) on February 21 and March 21 became open on February 22 and March 22. Other closed loops, for example, the large loops (yellow, on the left side), are reshaped into low-lying field lines (yellow, on the right side). A few of the field lines, which are open (blue) on the 21st, are remodeled into low- and high-closed magnetic loops on the 22nd.

4.2. Results of the NLFFF

We applied the NLFFF extrapolation to obtain the magnetic field configuration at the site of *Eruption 2*. The results for *Eruption 1* and *Eruption 3* did not reveal anything conclusive,

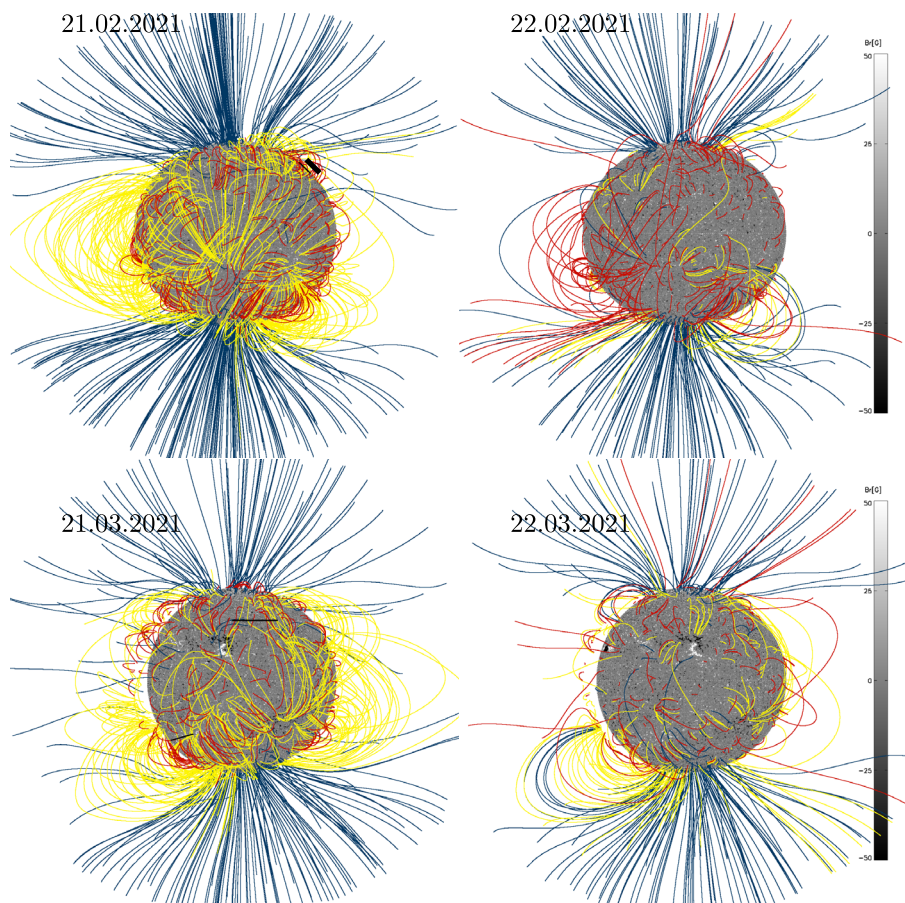


Figure 8 Traced loops from the PFSS solutions for February 21 and 22 (*top panels*) and for March 21 and 22 (*lower panels*). The position of the three prominences is marked by the *black straight lines* in the *left panels*. The *upper panels* were rotated such that *Eruption 1* is seen at the Northern-West limb in the *upper-left panel*. The view of the *upper panels* is from an observer situated at a Carrington longitude of 150 degrees (for orientation, see also the *top panel* of Figure 11). The *lower panels* show the view from approximately the Earth perspective (Carrington longitude of 300 degrees) (for orientation, see also the *bottom panel* of Figure 11). Note that in the *lower panels*, a portion of the eastern solar disk is missing. This is caused by the plotting program being unable to render that part of the solar disk from the synchronic map in Figure 11.

and, as a consequence, we do not show them here. For instance, *Eruption 1* was out of the FOV of the HMI vector magnetogram. The topology at the *Eruption 3* location shows an arcade-like shape of the magnetic field lines with no identifiable flux-rope-like shape. From the solution of the NLFFF extrapolation, we traced the field lines from which we plot some at the site of the eruptive prominence (*Eruption 2*). The position of the eruptive prominence is close to one of the lateral boundaries of the synchronic map (and implicit in the computational box), which makes difficult the evaluation of the surrounding magnetic field. In Figure 9, we show a zoom-in of the low-lying loops from different viewing perspectives. In Figure 10, we show the B_r component of the magnetic field at the bottom boundary, and on top, we overplot magnetic field lines. Not to overcrowd Figure 10, we excluded the low-lying loops (red, Figure 9). We display only the loops near the eruptive prominence. Some

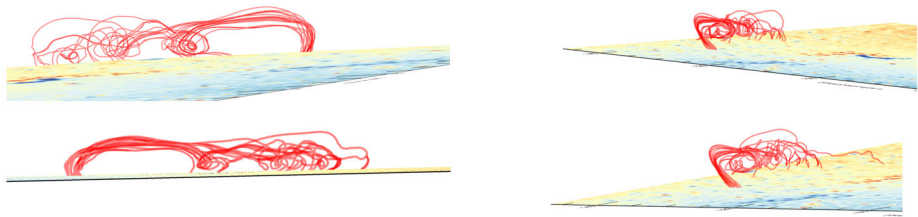


Figure 9 Zoom in of different views of the low lying magnetic field lines extrapolated using the solution of the NLFFF method for *Eruption 2*.

of the low-lying loops (red, pink) show helical twists, while some of the higher ones (pink, cyan, purple) are braided. The higher loops (orange, bright purple) are more potential. We also notice that some loops are abruptly cut, most probably because their continuation is out of the computational box.

5. Discussions

The visual aspect of the three prominence eruptions studied here is very different in EUV images taken from different perspectives (see Figure 1). This is most probably due to their extended nature and the respective positions of the spacecraft. The three prominences were observed on-disk in at least one view: *Eruption 1* in FSI, *Eruption 2* in AIA, and *Eruption 3* in EUVI-A. Such different views (on-disk and off-limb) help us understand their morphology better. However, at the same time, the different visual appearance resulted in difficulties in identifying the same feature when performing triangulation of the erupting feature close to the solar surface. Other effects like the asymmetric type of prominences, the LOS integration effect, the image contrast being different in the different instruments, etc., may have also contributed to the difficulty in identifying the same feature. For a detailed discussion on the correct identification and matching of features of an eruption in stereoscopic images see Inhester (2006) and Mierla et al. (2010).

The visual appearance of the corresponding CMEs in different coronagraphs is also different, as seen in Figure 7. However, the large-scale flux-rope model (the GCS model) used to match the data fits only the outer shell of the CME, mainly the leading edge (LE), which is well identifiable from the three perspectives. This resulted in the constraint of different properties of the CME. A more detailed discussion on the application of GCS to CMEs observed from different perspectives is provided in Thernisien, Vourlidis, and Howard (2011).

The GCS model has been successfully applied to CMEs observed by Metis (Andretta et al., 2021; Bemporad et al., 2022). Andretta et al. (2021) used the GCS model to analyze the first CME observed by Metis on January 16–17, 2021, which was a faint and slow stealth CME (i.e., a CME without low coronal signatures, Robbrecht, Patsourakos, and Vourlidis, 2009). It was observed from three different perspectives, with STEREO-A and Solar Orbiter being in opposition and the Earth at approximately the same angular distance between the two. The position of the spacecraft and the direction of propagation of the CME resembles the scenario of our *Eruption 1*, except that no prominence could be identified for that CME.

Similarly to our study, Bemporad et al. (2022) analyzed a complex sequence of three successive eruptive events that occurred between February 12–13, 2021: a slow and accelerated CME followed by a nearby prominence eruption and a trailing plasma blob. The authors applied three different reconstruction methods to the event: GCS for the main CME,

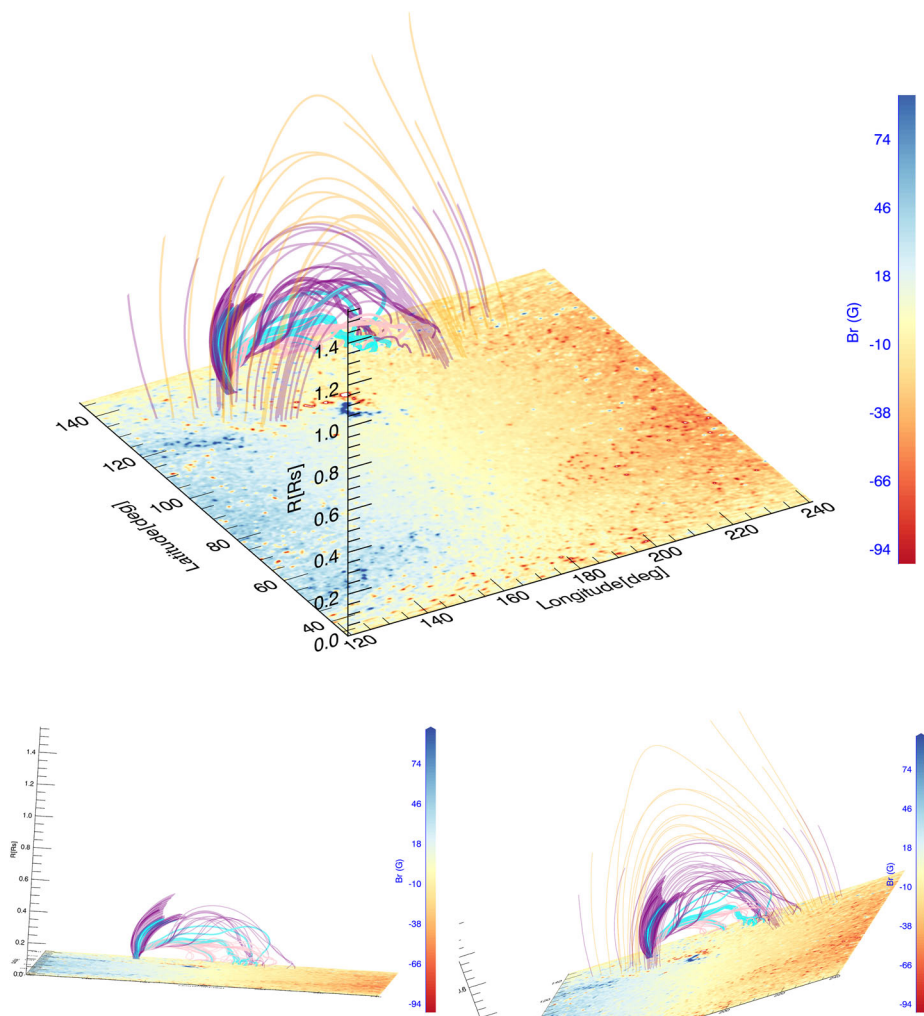


Figure 10 Magnetic-field lines extrapolated using the solution of the NLFFF method for *Eruption 2*. Different colors are used only for a better visualisation (see text for details).

triangulation for the erupting prominence, and polarisation ratio (Moran and Davila, 2004) for the trailing blob. Due to the large time difference between the CME and prominence eruption, the authors also concluded that these two events were fairly unrelated. Unlike their study, we applied the 3D reconstruction methods to the filaments and prominences that represented the sources of the CMEs, as well as to their corresponding CMEs. This allowed us to compare the evolution of the eruptions from low in the corona to larger heights.

The values derived from GCS show that *Eruption 1* and *Eruption 2* were deflected towards the equator by 25 degrees and 15 degrees, respectively, compared to their propagation direction derived from triangulation at lower heights, while *Eruption 3* only shows a slight deflection towards the equator and a stronger deflection towards the central meridian. The deflection of the first two eruptions was probably influenced by the nearby polar coronal holes. *Eruption 3* was flanked by two small coronal holes (CHs), of which the bigger one

to the east may have been responsible for the longitudinal deflection. Several authors have shown that open magnetic-field lines from CHs can act as magnetic walls causing the CMEs to deflect away from these structures (see, e.g., Cremades, Bothmer, and Tripathi, 2006; Panasenco et al., 2013; Cécere et al., 2020; Sieyra et al., 2020), while a streamer or a pseudostreamer can act as a potential well causing the CMEs to move towards them (see, e.g., Xie et al., 2009; Kay, Opher, and Evans, 2013; Liewer et al., 2015; Yang et al., 2018). In the case of the eruptions studied here, we could easily identify CHs close to the eruption sites, while the presence of streamers is more difficult to assess. From the PFSS analysis, it looks like *Eruption 2* and *Eruption 3* are located at the base of arcades of closed field lines, while *Eruption 1* looks to be located at the interface between open and closed field lines. NLFFF results also confirm that *Eruption 2* seems to be located at the base of an arcade of closed field lines. The PFSS results also indicate a strong change in the magnetic field configuration before and after the eruptions (see Figure 8). Some of the smooth low (red) and large loops (yellow) open up (blue), most probably as a result of the eruptions. A couple of the field lines, which were open, were remodeled into low- and high-closed magnetic loops after the eruptions. The NLFFF results for *Eruption 2* show significant helical twists in the low-lying loops (see Figure 9), while some of the higher ones are braided and the highest loops are more potential (see Figure 10).

6. Conclusions

This study shows the success of the application of 3D reconstruction techniques to prominences and CMEs observed from different perspectives and different distances to the Sun.

The prominences observed by different instruments in their 304 Å channels were extended and complex events with developed fine structures. This complicated the identification of the same feature observed by instruments from different perspectives in order to perform triangulation. The nature of the emission in 304 Å with both emitting and absorbing structures added an extra complexity in identifying the same part of a prominence. This was further complicated by the large passbands of the instruments, where more than one emission line is present. For instance, the FSI 304 Å images are dominated by the Ly- α He II emission line at 303.78 Å, but the passband also contains a number of weaker coronal lines, most prominently the Si XI line at 303.33 Å formed in the corona at temperatures around 2 MK (Labrosse and McGlinchey, 2012). Although a quantitative separation of coronal and prominence emission is difficult without spectroscopic observations, coronal (hot) and prominence (cool) structures can be qualitatively distinguished in the EUV images based on their morphology: smooth for the coronal features, ragged for prominence features. Triangulation may also provide a way to decouple LOS effects from the true emissivity effect (emission or absorption by cooler plasma) by assessing the true position of the prominence features. This is an area where the multi-viewpoint observations may lead to new insights.

The large-scale GCS reconstruction applied to the eruptions at higher heights proved to work well in constraining different aspects of the CMEs.

In order to compare the direction of propagation of these events at different coronal heights, we selected for triangulation only one point, which could be easily identified in two images taken from different perspectives, mostly the outer part of the prominence (Figure 6). These locations and heights (Table 3) were compared with the central part of the CME as derived from the GCS reconstruction (Table 4). For future studies, it will be interesting to reconstruct the full prominence in order to derive its entire 3D morphology.

From the solutions of the PFSS extrapolations, an apparent depletion in the global magnetic field after the eruptions was observed. The magnetic-field topology reconfigured after the eruptions, and maybe some of the large field lines reconnected into very small ones, undetected by the entire process of acquiring, processing, and modeling. For a more insightful explanation, a deeper investigation would be required. PFSS results near *Eruption 2* are not extremely reliable due to its vicinity to the active region NOAA 12810. Instead, the NLFFF results for this eruption show helical twists in the low-lying loops, while some of the higher ones are braided.

More observations from different locations (latitudes) will better constrain the reconstructions. Observations that will be taken by Solar Orbiter in the near future from different latitudes will shed new light on the morphology and propagation of the erupting prominences in three dimensions.

Appendix A: Detailed Description of the Observations

The three eruptions studied here, *Eruption 1*, *Eruption 2*, and *Eruption 3* are slow-rising prominences, spanning many degrees in longitude and latitude (see Table 2) and observed from three different perspectives (see Table 1): Earth perspective (at 1 AU), STEREO-A perspective (at 1 AU and 55 degrees East from the Earth) and Solar Orbiter perspective (at 0.5 AU and 0.7 AU, and 90 degrees and 55 degrees East of STEREO-A for *Eruption 1* and *Eruptions 2, 3*, respectively).

The three prominence eruptions were also observed by the Sun Watcher using Active Pixel (SWAP: Seaton et al., 2013) sensor onboard PROBA2 spacecraft and by the Solar Ultraviolet Imager (SUVI, Darnel et al., 2022) onboard the Geostationary Operational Environmental Satellite-16 (GOES-16).

All three eruptions could be seen in H-alpha images from the GONG network⁴ and the Kanzelhöhe Observatory.⁵ *Eruption 1* was seen as a small narrow prominence at NE limb in successive GONG H-alpha images at 07:37 UT and 15:42 UT on February 20 and at 01:49 UT on February 21. *Eruption 2* was observed as a very faint filament on-disk near central meridian at around 05:55 UT on March 21, and *Eruption 3* as a small filament close to the limb at SE at around 19:07 UT on March 21.

The position of the different spacecraft, and the direction of the three eruptions (as derived by means of the GCS method – see Section 3.2) are shown in Figure 2 (blue, green, and red arrows for *Eruption 1*, *Eruption 2* and *Eruption 3*, respectively). Their corresponding characteristics are presented in Tables 1 and 2.

On February 21 00:00 UT, Solar Orbiter was observing from a distance of 0.515 astronomical units (AU) from the Sun. This means that the difference in light travel time between Sun - Solar Orbiter and Sun - Earth is 3 minutes and 56 seconds, and between Sun - Solar Orbiter and Sun - STEREO-A is 3 minutes and 45 seconds.

On March 21 20:00 UT, Solar Orbiter was observing from a distance of 0.687 AU from the Sun. This means that the difference in light travel time between Sun - Solar Orbiter and Sun - Earth is 2 minutes and 34 seconds, and between Sun - Solar Orbiter and Sun - STEREO-A is 2 minutes and 19 seconds. All these temporal differences were taken in consideration when analyzing the three eruptions.

⁴gong2.nso.edu/products/tableView/table.php?configFile=configs/hAlpha.cfg.

⁵cesar.kso.ac.at/synoptic/ha_years.php.

A.1 Observations of Eruption 1

The first eruption (*Eruption 1*) started at around 00:00 UT on February 21 to the North-West (NW) of the Sun as seen from FSI. The prominence extends approximately from N40E75 to N40E105 in Stonyhurst coordinates. We calculated this approximate position by locating the position of one prominence/filament leg based on the dimming observed in the Extreme-Ultraviolet Imager (EUVI)-A 195 Å image at 10:00 UT (see explanations in the main text). We measured the size of the filament visible on-disk in an FSI 304 Å image at around 08:00 UT on February 21. We added this measured extent of 30 degrees to the position of the prominence leg. During the eruption, the filament is seen expanding 120 degrees Eastward in the FSI 304 Å movie.

Eruption 1 started at a high northern latitude, and it was deflected towards the equator. One extremity of the filament (*Ext1*) was seen off-limb (to the NW) from the Solar Orbiter perspective and the other extremity (*Ext2*) was seen on-disk, expanding towards the central meridian. *Ext1* was visible at the limb also from Earth's perspective while the *Ext2* was back-side from Earth's perspective. STEREO-A observed *Ext2* at the limb. *Ext1* should be seen erupting on-disk in STEREO-A/EUVI images, but the original movie does not show any evident motion. After further image processing to increase the contrast, one could observe a faint dark filament structure slowly erupting on-disk.

Later on, the prominence was observed as a three-part CME in the three coronagraphs from the three different perspectives.

A.2 Observations of Eruption 2

Eruption 2 was observed on March 21, starting around 11:00 UT to the NW of the Sun as seen from the Solar Orbiter perspective. The eruption started at a high northern latitude and was deflected towards the equator while erupting. It was well visible on-disk in AIA 304 Å spanning a longitudinal range of 30 degrees (from W00 to W30), at 10:00 UT, before it started to erupt (see Table 2). After around 19:00 UT, the erupting filament split in two, the left part going towards NE as far as to E35 and the right part going towards W-NW (as far as to W60). The eruption was back-sided from the Solar Orbiter's perspective and it was observed by FSI 304 Å at the NW limb. Material falling back to the Sun was observed starting around 21:00 UT. EUVI-A 304 Å observed the eruption both front- and back-sided at NW limb. The inflow material is clearly seen on the front side (E10N45 Stonyhurst coordinates).

Later on, the prominence was observed as a three-part CME by the three coronagraphs from the three different perspectives.

A.3 Observations of Eruption 3

Eruption 3 was observed on March 21 as a prominence to the South-West (SW) of the Sun as observed from Solar Orbiter perspective, starting to erupt at around 20:00 UT.

The same eruption was observed by EUVI-A 304 Å instrument at a high southern latitude as an extended filament (25 degrees in longitude at 22:00 UT on March 21). It started to erupt around 21:00 UT – 22:00 UT. The western leg appeared to disconnect first and the erupting material was going towards SE. FSI 304 Å observed the eruption on the front side at SW limb and AIA 304 Å observed it on the front side at SE limb. The western leg of the filament was closer to the limb, as observed by FSI, and the eastern leg was closer to the limb as observed by AIA. The shape of the prominence was different from the two perspectives.

The approximate location of *Eruption 3* at 22:00 UT was S40E55–S35E30 in Stonyhurst coordinates. The location was calculated from the EUVI-A 304 Å image when the filament

was identifiable on the solar disk. Note that the filament was not well observed on the solar disk at the beginning of the eruption (i.e., around 20:00 UT), and its size and position two hours later may be slightly different from its initial values.

The eruption was observed later on as a structured CME by LASCO-C2. It was a very faint CME, as observed by COR2-A. It was faint and narrow, as observed by Metis. A narrow ray-like feature was observed by LASCO-C2 before the CME, which appears to be dragged away by the CME.

A.4 Data Acquisition for Eruption 1

FSI instruments were observing on February 21 at a cadence of around 15 min (FSI 304 Å) and 8 min (FSI 174 Å), an exposure time of 10 sec, and a plate scale of about 1660 km per pixel. There were data gaps between February 20 22:54 UT and February 21 00:09 UT, and between 04:54 UT and 06:00 UT on February 21.

The EUVI-A 304 Å instrument was observing at a cadence of around 3 min, an exposure time of 4 sec and a plate scale of about 1114 km per pixel.

The AIA 304 Å instrument was observing at a cadence of around a few seconds, an exposure time of 2.9 sec and a plate scale of about 430 km per pixel.

On the same day, Metis was running a program in the context of the second Solar Orbiter Remote-Sensing Check-out Window (February 20–25, 2021). Both VL and UV channels were operating. In this work, we use data from the VL channel only. Each VL acquisition consisted of a set of four images each taken with a 30 sec exposure time and at a different polarization angle, the cycle being repeated 14 times. Each set of images acquired with the same polarization angle was then averaged on board; the resulting four images were combined on the ground to obtain a single polarized brightness (pB) image. The total acquisition time was therefore about 28 min, and the cadence of the image was slightly longer, about 29 min. All VL images were taken with a 4×4 binning leading to a plate scale of about 40 arcsecs or about 15000 km per pixel at a distance of 0.51 AU from the Sun. The data were calibrated and processed following the procedure outlined in Romoli et al. (2021). Despite the relatively long acquisition time, in the stream of interlaced images acquired on board, the polarization cycle lasts only 2 min, thus maximizing the reliability of the resulting pB. On the other hand, smearing effects for transients such as CMEs are not negligible: a feature moving at $\sim 100 \text{ km s}^{-1}$ would move by roughly 8–10 (binned) pixels during a single pB acquisition.

The LASCO-C2 instrument was observing at a cadence of around 12 min, an exposure time of 25 sec and a plate scale of about 8450 km per pixel. The COR2 instrument was observing at a cadence of around 15 min, an exposure time of 6 sec and a plate scale of about 10312 km per pixel.

A summary of the instrument characteristics is provided in Table 5.

A.5 Data Acquisition for Eruption 2 and Eruption 3

Both FSI telescopes were observing on March 21–22 at a cadence of around eight min, an exposure time of 10 sec and a plate scale of about 2199 km per pixel. There was a data gap between 04:55 UT to 07:02 UT on March 21 and from 04:55 UT to 12:17 UT on March 22.

AIA 304 Å instrument was observing at a cadence of around 12 sec, an exposure time of 2.9 sec and a plate scale of about 434 km per pixel.

EUVI-A 304 Å instrument was observing at a cadence of around 3 min, an exposure time of 4 sec and a plate scale of about 1114 km per pixel.

Table 5 Instrument characteristics on February 21, 2021. *The first column:* The instrument. *The second column:* image cadence. *The third column:* Image exposure time. *The fourth column:* Image plate scale. * The acquisition time of a pB sequence is 28 min (see text for details).

Instruments	Cadence [min]	Exposure time [sec]	Plate scale [km/pixel]
FSI 304 Å	15	10	1660
FSI 174 Å	8	10	1660
AIA 304 Å	12 sec	2.9	430
EUVI-A 304 Å	3	4	1114
Metis	29	30*	15000
LASCO-C2	12	25	8450
COR2	15	6	10312

Table 6 Instrument characteristics on March 21, 2021. *The first column:* The instrument. *The second column:* image cadence. *The third column:* Image exposure time. *The fourth column:* Image plate scale. * The acquisition time of a pB sequence is 28 min (see text for details).

Instruments	Cadence [min]	Exposure time [sec]	Plate scale [km/pixel]
FSI 304 Å	8	10	2199
FSI 174 Å	8	10	2199
AIA 304 Å	12 sec	2.9	434
EUVI-A 304 Å	3	4	1114
Metis	29	30*	20000
LASCO-C2	12	25	8510
COR2	15	6	10320

Metis observed in the context of the third Solar Orbiter Remote-Sensing Check-out Window (March 21–24, 2021); the acquisition parameters and processing steps for the VL channel were the same as described for *Eruption 1*. The plate scale in this case (at 0.69 AU) was about 20000 km per pixel.

LASCO-C2 instrument was observing at a cadence of around 12 min, an exposure time of 25 sec and a plate scale of about 8510 km per pixel. COR2 instrument was observing at a cadence of around 15 min, an exposure time of 6 sec and with a plate scale of about 10320 km per pixel.

A summary of the instrument characteristics is provided in Table 6.

Appendix B: Techniques used for the Magnetic Field Analysis

We are still challenged in obtaining the magnetic field in the solar corona. Therefore, the magnetic-field configuration in the higher layers of the atmosphere can be obtained with the help of different methods which extrapolate the magnetic field from the photosphere into the corona. One of the highly used extrapolation methods is PFSS. The reason is that PFSS, in comparison with other methods, has cheap computational demands, few constraints, and more reliable input data. One can obtain the potential magnetic field model for the coronal

magnetic field from Gauss theorem ($\nabla \cdot \mathbf{B} = 0$), by expressing the magnetic field as a function of scalar potential ϕ ($\mathbf{B} = -\nabla\phi$), and using the line-of-sight photospheric magnetic field component as boundary condition (Wiegelmann and Sakurai, 2012). With the PFSS, we obtain the lowest magnetic energy in the corona and a solution that contains no currents. It has been shown that before an eruption (Thalmann and Wiegelmann, 2008), the corona accumulates free energy, which is the magnetic energy building up on top of the potential energy. Not accounting for this free energy is a drawback of the PFSS method. Nevertheless, one can still make use of the information obtained from the solution of the PFSS method, like, e.g., the changes in time of the topology of the global magnetic field.

Another extrapolation method is NLFFF, which is much more computationally demanding and uses as input, data that sometimes are prone to larger errors (e.g., the transversal component of the magnetic field). The assumptions of the NLFFF are the existence of a regime where the magnetic pressure dominates over the plasma pressure and gravity, and a stationary plasma, which requires the lowest order of the Lorentz force to vanish. A nonlinear force-free magnetic field solution is found when the solenoidal condition ($\nabla \cdot \mathbf{B} = 0$) and the nonlinear equation $(\nabla \times \mathbf{B}) \times \mathbf{B} = 0$ are fulfilled. The advantage of the method is that the solution of the extrapolation complies best with observations (Tadesse et al., 2014) and gives an indication of the free energy accumulating in the solar corona before an eruption. It has been shown that using a larger FOV as input for the NLFFF method gives better results than smaller FOVs (Tadesse et al., 2013).

We applied the potential field method for obtaining the global magnetic field configuration before and after the three eruptions. We applied the NLFFF to obtain the magnetic field configuration at the site of the eruptions.

In the following subsection, we present the data used for the PFSS and the NLFFF extrapolations.

B.1 Data used for the Magnetic Field Analysis

For both of the magnetic field extrapolation methods, we used magnetic field data from SDO/HMI. The full disk HMI vector-magnetograms were first converted to the radial field (B_r) magnetograms by dividing by the cosine of the angle from the disk center. Individual radial magnetograms are then remapped and interpolated onto a very high-resolution Carrington coordinate grid using the Carrington Heliographic - Cylindrical Equal Area (CEA) projection (Sun, 2013). The extent in the longitude of the maps is 120 degrees centered at the central meridian and 114 degrees in latitude centered at the solar equator. We used HMI synchronic maps (see Figure 11) for the PFSS extrapolations and full disk vector magnetograms (see Figure 12) for the NLFFF extrapolation. In the radial r , longitudinal ϕ and latitudinal θ (r, θ, ϕ) extents, the computational box is $128 \times 360 \times 720$ grid points for the PFSS and $256 \times 476 \times 512$ grid points for the NLFFF.

The synchronic map is a combination of a standard synoptic map and a daily full disk map, and it is a data product suitable for the full-Sun extrapolation provided by the HMI team (Liu et al., 2017). Each longitude stripe of the standard synoptic map represents the average of 20 magnetograms obtained at the central meridian passage of that longitude. The synchronic frame, which represents data visible on the disk at one time, replaces a 120-degree longitude range of the data in the standard synoptic map. The synchronic frames are built daily using the daily magnetograms, between 10:00 UT and 14:00 UT, within a range of 60 degrees from the central meridian. The resulting magnetogram is an average of the 20 used magnetograms, which spans 120 degrees in longitude and is positioned at the left end of the final 360-degree synchronic map. In this way, that part of the synoptic frame better represents the fast evolving magnetic features.

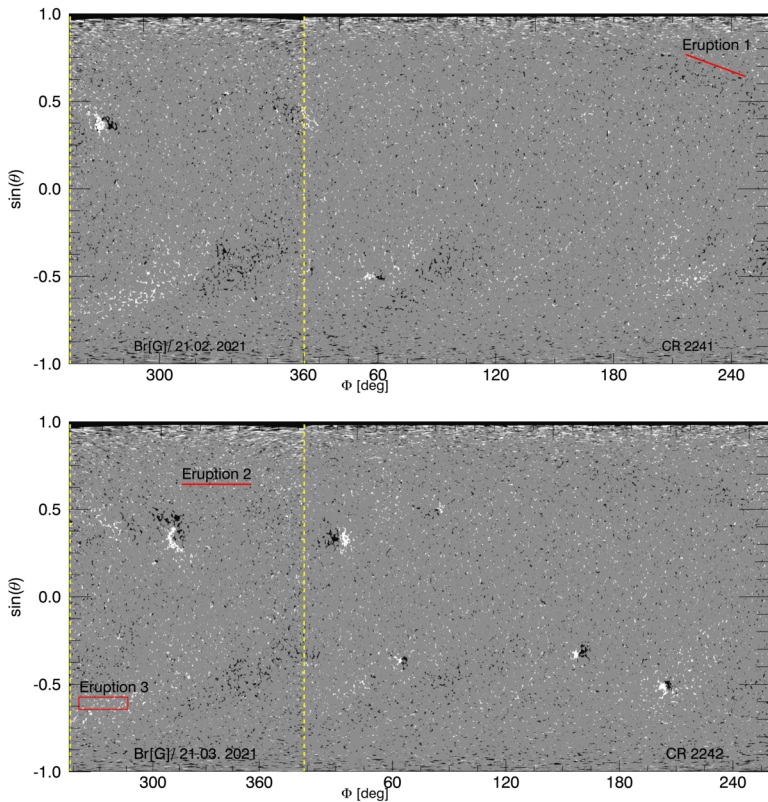


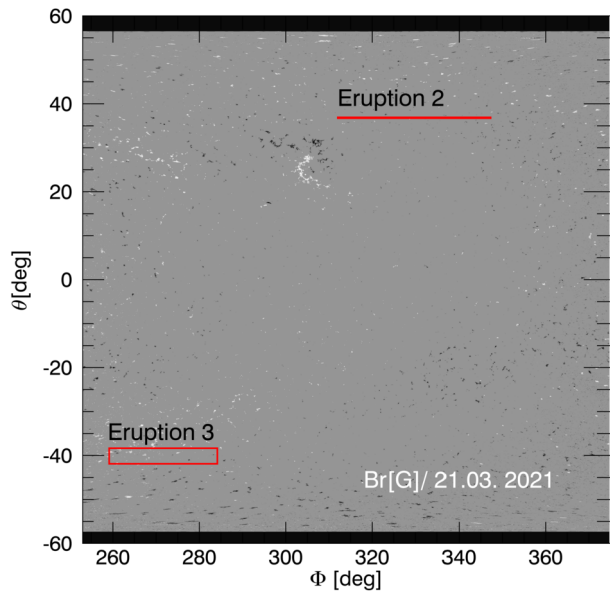
Figure 11 The Br component of the magnetic field from SDO/HMI, for the synchronic magnetic field maps on February 21 (*top panel*) and March 21 (*lower panel*) 2021. The synoptic map for February (Carrington Rotation 2241) starts on February 18 and ends on March 17, and the synoptic map for March (Carrington Rotation 2242) starts on March 17 and ends on April 14. Synchronic frames (delimited by the *vertical dashed lines*, i.e., the left side of the synoptic map) replace a 120-degree longitude range of the data in the synoptic maps with data observed at a given time (February 21 *upper panel* and March 21 *lower panel*). The *red marks* represent the position of the three prominences as given in Table 2. The location of *Eruption 1* (*upper panel*) is out of the synchronic Br map. X-axis is longitude, and Y-axis is latitude in Carrington coordinates.

In Figure 11, we show the radial component of the synchronic magnetic field maps for February 21 (*upper panel*) and March 21 (*lower panel*). The magnetic field is saturated at ± 50 G for a better visualization. The red boxes/lines indicate the approximate location of the eruptive prominences (*Eruption 2* to the North and *Eruption 3* to the South) in the lower panel of Figure 11. The location of *Eruption 1* is out of the synchronic Br map (*upper panel* of Figure 11).

The map used for NLFFF extrapolation is shown in Figure 12. The red marks indicate the approximate location of the eruptive prominences (*Eruption 2* at North and *Eruption 3* at South). To have consistent boundary conditions for the NLFFF method, we applied the pre-processing of the data using the method described by Tadesse, Wiegelmann, and Inhester (2009).

Acknowledgments Solar Orbiter is a space mission of international collaboration between ESA and NASA, operated by ESA. The EUFI instrument was built by CSL, IAS, MPS, MSSL/UCL, PMOD/WRC, ROB, LCF/IO with funding from the Belgian Federal Science Policy Office (BELSPO/PRODEX PEA

Figure 12 The Br component of the magnetic field from SDO/HMI, for a selected region of the full disk on the 21 March 2021. The red marks represent the position of the prominence 2 and prominence 3 as given in Table 2. X-axis is longitude and Y-axis is latitude in Carrington coordinates.



4000134088); the Centre National d'Etudes Spatiales (CNES); the UK Space Agency (UKSA); the Bundesministerium für Wirtschaft und Energie (BMWi) through the Deutsches Zentrum für Luft- und Raumfahrt (DLR); and the Swiss Space Office (SSO). The Metis programme is supported by the Italian Space Agency (ASI) under the contracts to the co-financing National Institute of Astrophysics (INAF): Accordi ASI-INAF N. I-043-10-0 and Addendum N. I-013-12-0/1, Accordo ASI-INAF N.2018-30-HH.0 and under the contracts to the industrial partners OHB Italia SpA, Thales Alenia Space Italia SpA and ALTEC: ASI-TASI N. I-037-11-0 and ASI-ATI N. 2013-057-I.0. Metis was built with hardware contributions from Germany (Bundesministerium für Wirtschaft und Energie (BMWi) through the Deutsches Zentrum für Luft- und Raumfahrt e.V. (DLR)), from the Academy of Sciences of the Czech Republic (Czech PRODEX) and from ESA. We acknowledge the use of Solar Orbiter/EUI, Solar Orbiter/Metis, PROBA2/SWAP, SDO/AIA, SOHO/LASCO, and STEREO/EUVI, COR2 data. The LASCO CME catalogue used in this study is generated and maintained at the CDAW Data Center by NASA and The Catholic University of America in cooperation with the Naval Research Laboratory. SOHO is a project of international cooperation between ESA and NASA.

Author contributions All authors participated in analyzing the three prominence eruptions and their corresponding CMEs. M.M. performed the 3D reconstruction of prominences. H.C. performed the 3D reconstruction of CMEs. I.C. performed the magnetic field extrapolation. A.N.Z., F.A., A.V., D.C.T., L.R., J.J., R.A.C., E.DH., L.D., D.M.L., C.M., P.P., S.P., M.J.W., O.P., L.T., W.T., E.D. contributed to the analysis of the observations and to the interpretation of the results. B.N., D.B., S.G., E.K., B.M., K.S., C.V. contributed to the processing and analysis of FSI data. V.A., R.S., A.B., G.J., M.R., C.S. contributed to the processing and analysis of Metis data. D.C.T. made the FSI movies. A.V. made the Metis movies. M.M., H.C. and I.C. wrote the main manuscript text. All authors reviewed the manuscript.

Funding Open Access funding enabled and organized by Projekt DEAL. The ROB team thanks the Belgian Federal Science Policy Office (BELSPO) for the provision of financial support in the framework of the PRODEX Programme of the European Space Agency (ESA) under contract numbers 4000134474, 4000134088, and 4000136424. D.M.L. is grateful to the Science Technology and Facilities Council for the award of an Ernest Rutherford Fellowship (ST/R003246/1). I.C. acknowledges the support of the Coronagraphic German and US Solar Probe Plus Survey (CGAUSS) project for WISPR by the German Aerospace Center (DLR) under grant 50OL1901 as a national contribution to the Parker Solar Probe mission. A.V. is supported by SoloHI and WISPR Phase-E funds. H.C. is a member of "Carrera del Investigador Científico" of CONICET and acknowledges funding from PIP11220200102710 (CONICET) and MSTCAME8181TC (UTN). C. M. is funded by the European Union (ERC, HELIO4CAST, 101042188). Views and opinions expressed are, however, those of the author(s) only and do not necessarily reflect those of the European Union

or the European Research Council Executive Agency. Neither the European Union nor the granting authority can be held responsible for them.

Data Availability All the data used in this study (Solar Orbiter/EUI, Solar Orbiter/Metis, SDO/AIA, SDO/HMI, PROBA2/SWAP, SECCHI-EUVI, -COR2, and SOHO/LASCO-C2 and GOES-16/SUVI) are publicly available and, with the exception of Metis data, can be downloaded from the corresponding instrument webpages. Metis data are available upon request from the instrument PI; work is in progress to make Metis data available on the Solar Orbiter Archive (SOAR).

Declarations

Competing interests The authors declare no competing interests.

Open Access This article is licensed under a Creative Commons Attribution 4.0 International License, which permits use, sharing, adaptation, distribution and reproduction in any medium or format, as long as you give appropriate credit to the original author(s) and the source, provide a link to the Creative Commons licence, and indicate if changes were made. The images or other third party material in this article are included in the article's Creative Commons licence, unless indicated otherwise in a credit line to the material. If material is not included in the article's Creative Commons licence and your intended use is not permitted by statutory regulation or exceeds the permitted use, you will need to obtain permission directly from the copyright holder. To view a copy of this licence, visit <http://creativecommons.org/licenses/by/4.0/>.

References

- Altschuler, M.D., Newkirk, G.: 1969, Magnetic fields and the structure of the Solar Corona. I: methods of calculating coronal fields. *Solar Phys.* **9**, 131. [DOI](#). [ADS](#).
- Andretta, V., Bemporad, A., De Leo, Y., Jerse, G., Landini, F., Mierla, M., Naletto, G., Romoli, M., Sasso, C., Slemer, A., Spadaro, D., Susino, R., Talpeanu, D.-C., Telloni, D., Teriaca, L., Uslenghi, M., Antonucci, E., Auchère, F., Berghmans, D., Berlicki, A., Capobianco, G., Capuano, G.E., Casini, C., Casti, M., Chioetto, P., Da Deppo, V., Fabi, M., Fineschi, S., Frassati, F., Frassetto, F., Giordano, S., Grimani, C., Heinzel, P., Liberatore, A., Magli, E., Massone, G., Messerotti, M., Moses, D., Nicolini, G., Pancrazzi, M., Pelizzo, M.-G., Romano, P., Schühle, U., Stangalini, M., Straus, T., Volpicelli, C.A., Zangrilli, L., Zuppella, P., Abbo, L., Aznar Cuadrado, R., Bruno, R., Ciaravella, A., D'Amicis, R., Lamy, P., Lanzafame, A., Malvezzi, A.M., Nicolosi, P., Nisticò, G., Peter, H., Plainaki, C., Poletto, L., Reale, F., Solanki, S.K., Strachan, L., Tondello, G., Tsinganos, K., Velli, M., Ventura, R., Vial, J.-C., Woch, J., Zimbardo, G.: 2021, The first coronal mass ejection observed in both visible-light and UV H I Ly- α channels of the Metis coronagraph on board Solar Orbiter. *Astron. Astrophys.* **656**, L14. [DOI](#). [ADS](#).
- Antonucci, E., Romoli, M., Andretta, V., Fineschi, S., Heinzel, P., Moses, J.D., Naletto, G., Nicolini, G., Spadaro, D., Teriaca, L., Berlicki, A., Capobianco, G., Crescenzo, G., Da Deppo, V., Focardi, M., Frassetto, F., Heerlein, K., Landini, F., Magli, E., Marco Malvezzi, A., Massone, G., Melich, R., Nicolosi, P., Noci, G., Pancrazzi, M., Pelizzo, M.G., Poletto, L., Sasso, C., Schühle, U., Solanki, S.K., Strachan, L., Susino, R., Tondello, G., Uslenghi, M., Woch, J., Abbo, L., Bemporad, A., Casti, M., Dolei, S., Grimani, C., Messerotti, M., Ricci, M., Straus, T., Telloni, D., Zuppella, P., Auchère, F., Bruno, R., Ciaravella, A., Corso, A.J., Alvarez Copano, M., Aznar Cuadrado, R., D'Amicis, R., Enge, R., Gravina, A., Jejičić, S., Lamy, P., Lanzafame, A., Meierdierks, T., Papagiannaki, I., Peter, H., Fernandez Rico, G., Giday Sertsu, M., Staub, J., Tsinganos, K., Velli, M., Ventura, R., Verroi, E., Vial, J.-C., Vives, S., Volpicelli, A., Werner, S., Zerr, A., Negri, B., Castronuovo, M., Gabrielli, A., Bertacin, R., Carpentiero, R., Natalucci, S., Marliani, F., Cesa, M., Laget, P., Morea, D., Pieraccini, S., Radaelli, P., Sandri, P., Sarra, P., Cesare, S., Del Forno, F., Massa, E., Montabone, M., Mottini, S., Quattropiani, D., Schillaci, T., Boccardo, R., Brando, R., Pandi, A., Baietto, C., Bertone, R., Alvarez-Herrero, A., García Parejo, P., Cebollero, M., Amoroso, M., Centonze, V.: 2020, Metis: the Solar Orbiter visible light and ultraviolet coronal imager. *Astron. Astrophys.* **642**, A10. [DOI](#). [ADS](#).
- Auchère, F., Andretta, V., Antonucci, E., Bach, N., Battaglia, M., Bemporad, A., Berghmans, D., Buchlin, E., Caminade, S., Carlsson, M., Carlyle, J., Cerullo, J.J., Chamberlin, P.C., Colaninno, R.C., Davila, J.M., De Groof, A., Etesi, L., Fahmy, S., Fineschi, S., Fludra, A., Gilbert, H.R., Giunta, A., Grundy, T., Haber-reiter, M., Harra, L.K., Hassler, D.M., Hirzberger, J., Howard, R.A., Hurford, G., Kleint, L., Kolleck, M., Krucker, S., Lagg, A., Landini, F., Long, D.M., Lefort, J., Lodiot, S., Mampaey, B., Maloney, S.,

- Marliani, F., Martinez-Pillet, V., McMullin, D.R., Müller, D., Nicolini, G., Orozco Suarez, D., Pacros, A., Pancrazzi, M., Parenti, S., Peter, H., Philippon, A., Plunkett, S., Rich, N., Rochus, P., Rouillard, A., Romoli, M., Sanchez, L., Schühle, U., Sidher, S., Solanki, S.K., Spadaro, D., St Cyr, O.C., Straus, T., Tanco, I., Teriaca, L., Thompson, W.T., del Toro Iniesta, J.C., Verbeeck, C., Vourlidas, A., Watson, C., Wiegelmann, T., Williams, D., Woch, J., Zhukov, A.N., Zouganelis, I.: 2020, Coordination within the remote sensing payload on the Solar Orbiter mission. *Astron. Astrophys.* **642**, A6. DOI. ADS.
- Bemporad, A., Andretta, V., Susino, R., Mancuso, S., Spadaro, D., Mierla, M., Berghmans, D., D’Huys, E., Zhukov, A.N., Talpeanu, D.-C., Colaninno, R., Hess, P., Koza, J., Jejcic, S., Heinzel, P., Antonucci, E., Da Deppo, V., Fineschi, S., Frassati, F., Jerse, G., Landini, F., Naletto, G., Nicolini, G., Pancrazzi, M., Romoli, M., Sasso, C., Slemer, A., Stangalini, M., Teriaca, L.: 2022, Coronal mass ejection followed by a prominence eruption and a plasma blob as observed by Solar Orbiter. *Astron. Astrophys.* **665**, A7. DOI. ADS.
- Braga, C., Vourlidas, A., Liewer, P., Hess, P., Stenborg, G.: 2021, Coronal mass ejection distortion at 0.1 au observed by WISPR. In: *AGU Fall Meeting Abstracts 2021*, SH42A. ADS.
- Brueckner, G.E., Howard, R.A., Koomen, M.J., Korendyke, C.M., Michels, D.J., Moses, J.D., Socker, D.G., Dere, K.P., Lamy, P.L., Llebaria, A., Bout, M.V., Schwenn, R., Simnett, G.M., Bedford, D.K., Eyles, C.J.: 1995, The large angle spectroscopic coronagraph (LASCO). *Solar Phys.* **162**, 357. DOI. ADS.
- Cécere, M., Sieyra, M.V., Cremades, H., Mierla, M., Sahade, A., Stenborg, G., Costa, A., West, M.J., D’Huys, E.: 2020, Large non-radial propagation of a coronal mass ejection on 2011 January 24. *Adv. Space Res.* **65**, 1654. DOI. ADS.
- Cremades, H., Bothmer, V., Tripathi, D.: 2006, Properties of structured coronal mass ejections in solar cycle 23. *Adv. Space Res.* **38**, 461. DOI. ADS.
- Darnel, J.M., Seaton, D.B., Bethge, C., Rachmeler, L., Jarvis, A., Hill, S.M., Peck, C.L., Hughes, J.M., Shapiro, J., Riley, A., Vasudevan, G., Shing, L., Koener, G., Edwards, C., Mathur, D., Timothy, S.: 2022, The GOES-R solar UltraViolet imager. *Space Weather* **20**, e2022SW003044. DOI. ADS.
- Domingo, V., Fleck, B., Poland, A.I.: 1995, The SOHO mission: an overview. *Solar Phys.* **162**, 1. DOI. ADS.
- Dryer, M., Liou, K., Wu, C., Wu, S., Rich, N., Plunkett, S.P., Simpson, L., Fry, C.D., Schenk, K.: 2012, Extreme fast coronal mass ejection on 23 July 2012. In: *AGU Fall Meeting Abstracts 2012*, SH44B. ADS.
- Fox, N.J., Velli, M.C., Bale, S.D., Decker, R., Driesman, A., Howard, R.A., Kasper, J.C., Kinnison, J., Kusterer, M., Lario, D., Lockwood, M.K., McComas, D.J., Raouafi, N.E., Szabo, A.: 2016, The solar probe plus mission: humanity’s first visit to our star. *Space Sci. Rev.* **204**, 7. DOI. ADS.
- Gibson, S.E.: 2018, Solar prominences: theory and models. Fleshing out the magnetic skeleton. *Living Rev. Solar Phys.* **15**, 7. DOI. ADS.
- Howard, R.A., Moses, J.D., Vourlidas, A., Newmark, J.S., Socker, D.G., Plunkett, S.P., Korendyke, C.M., Cook, J.W., Hurley, A., Davila, J.M., Thompson, W.T., St Cyr, O.C., Mentzell, E., Mehalick, K., Lemen, J.R., Wuelsel, J.P., Duncan, D.W., Tarbell, T.D., Wolfson, C.J., Moore, A., Harrison, R.A., Waltham, N.R., Lang, J., Davis, C.J., Eyles, C.J., Mapson-Menard, H., Simnett, G.M., Halain, J.P., Defise, J.M., Mazy, E., Rochus, P., Mercier, R., Ravet, M.F., Delmotte, F., Auchere, F., Delaboudiniere, J.P., Bothmer, V., Deutsch, W., Wang, D., Rich, N., Cooper, S., Stephens, V., Maahs, G., Baugh, R., McMullin, D., Carter, T.: 2008, Sun Earth Connection Coronal and Heliospheric Investigation (SECCHI). *Space Sci. Rev.* **136**, 67. DOI. ADS.
- Hrazdíra, Z., Druckmüller, M., Habbal, S.: 2021, Measuring solar differential rotation with an iterative phase correlation method. *Astrophys. J. Suppl.* **252**, 6. DOI. ADS.
- Hundhausen, A.J., Burckpile, J.T., St. Cyr, O.C.: 1994, Speeds of coronal mass ejections: SMM observations from 1980 and 1984-1989. *J. Geophys. Res.* **99**, 6543. DOI. ADS.
- Illing, R.M.E., Hundhausen, A.J.: 1986, Disruption of a coronal streamer by an eruptive prominence and coronal mass ejection. *J. Geophys. Res.* **91**, 10951. DOI. ADS.
- Inhester, B.: 2006, Stereoscopia basics for the STEREO mission. arXiv e-prints. astro. ADS.
- Kaiser, M.L., Kucera, T.A., Davila, J.M., St. Cyr, O.C., Guhathakurta, M., Christian, E.: 2008, The STEREO mission: an introduction. *Space Sci. Rev.* **136**, 5. DOI. ADS.
- Kay, C., Opher, M., Evans, R.M.: 2013, Forecasting a coronal mass ejection’s altered trajectory: ForeCAT. *Astrophys. J.* **775**, 5. DOI. ADS.
- Labrosse, N., McGlinchey, K.: 2012, Plasma diagnostic in eruptive prominences from SDO/AIA observations at 304 Å. *Astron. Astrophys.* **537**, A100. DOI. ADS.
- Lemen, J.R., Title, A.M., Akin, D.J., Boerner, P.F., Chou, C., Drake, J.F., Duncan, D.W., Edwards, C.G., Friedlaender, F.M., Heyman, G.F., Hurlburt, N.E., Katz, N.L., Kushner, G.D., Levay, M., Lindgren, R.W., Mathur, D.P., McFeaters, E.L., Mitchell, S., Rehse, R.A., Schrijver, C.J., Springer, L.A., Stern, R.A., Tarbell, T.D., Wuelsel, J.-P., Wolfson, C.J., Yanari, C., Bookbinder, J.A., Chemists, P.N., Caldwell, D., Deluca, E.E., Gates, R., Golub, L., Park, S., Podgorski, W.A., Bush, R.I., Scherrer, P.H., Gummin, M.A., Smith, P., Auker, G., Jerram, P., Pool, P., Soufli, R., Windt, D.L., Beardsley, S., Clapp, M., Lang,

- J., Waltham, N.: 2012, The Atmospheric Imaging Assembly (AIA) on the Solar Dynamics Observatory (SDO). *Solar Phys.* **275**, 17. DOI. ADS.
- Liewer, P., Panasenco, O., Vourlidis, A., Colaninno, R.: 2015, Observations and analysis of the non-radial propagation of coronal mass ejections near the sun. *Solar Phys.* **290**, 3343. DOI. ADS.
- Liou, K., Wu, C.-C., Dryer, M., Wu, S.-T., Rich, N., Plunkett, S., Simpson, L., Fry, C.D., Schenk, K.: 2014, Global simulation of extremely fast coronal mass ejection on 23 July 2012. *J. Atmos. Solar-Terr. Phys.* **121**, 32. DOI. ADS.
- Liu, Y., Hoeksema, J.T., Sun, X., Hayashi, K.: 2017, Vector magnetic field synoptic charts from the Helioseismic and Magnetic Imager (HMI). *Solar Phys.* **292**, 29. DOI.
- Mierla, M., Inhester, B., Antunes, A., Boursier, Y., Byrne, J.P., Colaninno, R., Davila, J., de Koning, C.A., Gallagher, P.T., Gissot, S., Howard, R.A., Howard, T.A., Kramar, M., Lamy, P., Liewer, P.C., Maloney, S., Marqué, C., McAteer, R.T.J., Moran, T., Rodriguez, L., Srivastava, N., St. Cyr, O.C., Stenborg, G., Temmer, M., Thernisien, A., Vourlidis, A., West, M.J., Wood, B.E., Zhukov, A.N.: 2010, On the 3-D reconstruction of Coronal Mass Ejections using coronagraph data. *Ann. Geophys.* **28**, 203. DOI. ADS.
- Mierla, M., Zhukov, A.N., Berghmans, D., Parenti, S., Auchère, F., Heinzel, P., Seaton, D.B., Palmerio, E., Jejičić, S., Janssens, J., Kraaikamp, E., Nicula, B., Long, D.M., Hayes, L.A., Jebaraj, I.C., Talpeanu, D.-C., D’Huys, E., Dolla, L., Gissot, S., Magdalenic, J., Rodriguez, L., Shestov, S., Stegen, K., Verbeeck, C., Sasso, C., Romoli, M., Andretta, V.: 2022, Prominence eruption observed in He II 304 Å up to $>6 R_{\odot}$ by EU/FSI aboard Solar Orbiter. *Astron. Astrophys.* **662**, L5. DOI. ADS.
- Moran, T.G., Davila, J.M.: 2004, Three-dimensional polarimetric imaging of coronal mass ejections. *Science* **305**, 66. DOI. ADS.
- Müller, D., St. Cyr, O.C., Zouganelis, I., Gilbert, H.R., Marsden, R., Nieves-Chinchilla, T., Antonucci, E., Auchère, F., Berghmans, D., Horbury, T.S., Howard, R.A., Krucker, S., Maksimovic, M., Owen, C.J., Rochus, P., Rodriguez-Pacheco, J., Romoli, M., Solanki, S.K., Bruno, R., Carlsson, M., Fludra, A., Harra, L., Hassler, D.M., Livì, S., Louarn, P., Peter, H., Schühle, U., Teriaca, L., del Toro Iniesta, J.C., Wimmer-Schweingruber, R.F., Marsch, E., Velli, M., De Groof, A., Walsh, A., Williams, D.: 2020, The Solar Orbiter mission. Science overview. *Astron. Astrophys.* **642**, A1. DOI. ADS.
- Panasenco, O., Martin, S.F., Velli, M., Vourlidis, A.: 2013, Origins of rolling, twisting, and non-radial propagation of eruptive solar events. *Solar Phys.* **287**, 391. DOI. ADS.
- Pesnel, W.D., Thompson, B.J., Chamberlin, P.C.: 2012, The Solar Dynamics Observatory (SDO). *Solar Phys.* **275**, 3. DOI. ADS.
- Robbrecht, E., Patsourakos, S., Vourlidis, A.: 2009, No trace left behind: STEREO observation of a coronal mass ejection without low coronal signatures. *Astrophys. J.* **701**, 283. DOI. ADS.
- Rochus, P., Auchère, F., Berghmans, D., Harra, L., Schmutz, W., Schühle, U., Addison, P., Appourchaux, T., Aznar Cuadrado, R., Baker, D., Barbay, J., Bates, D., BenMoussa, A., Bergmann, M., Beurthe, C., Borgo, B., Bonte, K., Bouzit, M., Bradley, L., Büchel, V., Buchlin, E., Büchner, J., Cabé, F., Cadiergues, L., Chaigneau, M., Chares, B., Choque Cortez, C., Coker, P., Condamine, M., Coumar, S., Curdt, W., Cutler, J., Davies, D., Davison, G., Defise, J.-M., Del Zanna, G., Delmotte, F., Delouille, V., Dolla, L., Dumesnil, C., Dürig, F., Enge, R., François, S., Fourmond, J.-J., Gillis, J.-M., Giordanengo, B., Gissot, S., Green, L.M., Guerreiro, N., Guilbaud, A., Gyo, M., Haberreiter, M., Hafiz, A., Hailey, M., Halain, J.-P., Hansotte, J., Hecquet, C., Heerlein, K., Hellin, M.-L., Hemsley, S., Hermans, A., Hervier, V., Hochedez, J.-F., Houbrechts, Y., Ihsan, K., Jacques, L., Jérôme, A., Jones, J., Kahle, M., Kennedy, T., Klaproth, M., Kolleck, M., Koller, S., Kotsialos, E., Kraaikamp, E., Langer, P., Lawrenson, A., Le Clech’, J.-C., Lenaerts, C., Liebecq, S., Linder, D., Long, D.M., Mampaey, B., Markiewicz-Innes, D., Marquet, B., Marsch, E., Matthews, S., Mazy, E., Mazzoli, A., Meining, S., Meltchakov, E., Mercier, R., Meyer, S., Monecke, M., Monfort, F., Morinaud, G., Moron, F., Mountney, L., Müller, R., Nicula, B., Parenti, S., Peter, H., Pfflner, D., Philippon, A., Phillips, I., Plessiera, J.-Y., Plysser, E., Rabecki, F., Ravet-Krill, M.-F., Rebellato, J., Renotte, E., Rodriguez, L., Roose, S., Rosin, J., Rossi, L., Roth, P., Rouesnel, F., Roulliy, M., Rousseau, A., Ruane, K., Scanlan, J., Schlatter, P., Seaton, D.B., Silliman, K., Smit, S., Smith, P.J., Solanki, S.K., Spescha, M., Spencer, A., Stegen, K., Stockman, Y., Swzec, N., Tamiatto, C., Tandy, J., Teriaca, L., Theobald, C., Tychon, I., van Driel-Gesztelyi, L., Verbeeck, C., Vial, J.-C., Werner, S., West, M.J., Westwood, D., Wiegelmann, T., Willis, G., Winter, B., Zerr, A., Zhang, X., Zhukov, A.N.: 2020, The Solar Orbiter EUV instrument: the extreme ultraviolet imager. *Astron. Astrophys.* **642**, A8. DOI. ADS.
- Romoli, M., Antonucci, E., Andretta, V., Capuano, G.E., Da Deppo, V., De Leo, Y., Downs, C., Fineschi, S., Heinzel, P., Landini, F., Liberatore, A., Nalletto, G., Nicolini, G., Pancrazzi, M., Sasso, C., Spadaro, D., Susino, R., Telsoni, D., Teriaca, L., Uslenghi, M., Wang, Y.-M., Bemporad, A., Capobianco, G., Casti, M., Fabi, M., Frassati, F., Frassetto, F., Giordano, S., Grimani, C., Jerse, G., Magli, E., Massone, G., Messerotti, M., Moses, D., Pelizzo, M.-G., Romano, P., Schühle, U., Slemser, A., Stangalini, M., Straus, T., Volpicelli, C.A., Zangrilli, L., Zuppella, P., Abbo, L., Auchère, F., Aznar Cuadrado, R., Berlicki, A., Bruno, R., Ciaravella, A., D’Amicis, R., Lamy, P., Lanzafame, A., Malvezzi, A.M., Nicolosi, P., Nisticò,

- G., Peter, H., Plainaki, C., Poletto, L., Reale, F., Solanki, S.K., Strachan, L., Tondello, G., Tsinganos, K., Velli, M., Ventura, R., Vial, J.-C., Woch, J., Zimbardo, G.: 2021, First light observations of the solar wind in the outer corona with the Metis coronagraph. *Astron. Astrophys.* **656**, A32. DOI ADS.
- Santandrea, S., Gantois, K., Strauch, K., Teston, F., Tilmans, E., Baijot, C., Gerrits, D., De Groof, A., Schwehm, G., Zender, J.: 2013, PROBA2: mission and spacecraft overview. *Solar Phys.* **286**, 5. DOI ADS.
- Schou, J., Scherrer, P.H., Bush, R.I., Wachter, R., Couvidat, S., Rabello-Soares, M.C., Bogart, R.S., Hoeksema, J.T., Liu, Y., Duvall, T.L., Akin, D.J., Allard, B.A., Miles, J.W., Rairden, R., Shine, R.A., Tarbell, T.D., Title, A.M., Wolfson, C.J., Elmore, D.F., Norton, A.A., Tomczyk, S.: 2012, Design and ground calibration of the Helioseismic and Magnetic Imager (HMI) instrument on the Solar Dynamics Observatory (SDO). *Solar Phys.* **275**, 229. DOI ADS.
- Schrijver, C.J., De Rosa, M.L.: 2003, Photospheric and heliospheric magnetic fields. *Solar Phys.* **212**, 165. DOI ADS.
- Seaton, D.B., Berghmans, D., Nicula, B., Halain, J.-P., De Groof, A., Thibert, T., Bloomfield, D.S., Raftery, C.L., Gallagher, P.T., Auchère, F., Defise, J.-M., D’Huys, E., Lecat, J.-H., Mazy, E., Rochus, P., Rossi, L., Schühle, U., Slemzin, V., Yalim, M.S., Zender, J.: 2013, The SWAP EUV imaging telescope Part I: instrument overview and pre-flight testing. *Solar Phys.* **286**, 43. DOI ADS.
- Sieyra, M.V., Cécere, M., Cremades, H., Iglesias, F.A., Sahade, A., Mierla, M., Stenborg, G., Costa, A., West, M.J., D’Huys, E.: 2020, Analysis of large deflections of prominence-CME events during the rising phase of solar cycle 24. *Solar Phys.* **295**, 126. DOI ADS.
- Sun, X.: 2013, On the Coordinate System of Space-Weather HMI Active Region Patches (SHARPs): A Technical Note. arXiv e-prints. arXiv ADS.
- Tadesse, T., Wiegelmann, T., Inhester, B.: 2009, Nonlinear force-free coronal magnetic field modelling and preprocessing of vector magnetograms in spherical geometry. *Astron. Astrophys.* **508**, 421. DOI ADS.
- Tadesse, T., Wiegelmann, T., Inhester, B., Pevtsov, A.: 2011, Nonlinear force-free field extrapolation in spherical geometry: improved boundary data treatment applied to a SOLIS/VSM vector magnetogram. *Astron. Astrophys.* **527**, A30.
- Tadesse, T., Wiegelmann, T., MacNeice, P.J., Olson, K.: 2013, Modeling coronal magnetic field using spherical geometry: cases with several active regions. *Astrophys. Space Sci.* **347**, 21. DOI ADS.
- Tadesse, T., Wiegelmann, T., MacNeice, P.J., Inhester, B., Olson, K., Pevtsov, A.: 2014, A comparison between nonlinear force-free field and potential field models using full-disk SDO/HMI magnetogram. *Solar Phys.* **289**, 831. DOI ADS.
- Thalmann, J.K., Wiegelmann, T.: 2008, Evolution of the flaring active region NOAA 10540 as a sequence of nonlinear force-free field extrapolations. *Astron. Astrophys.* **484**, 495. DOI ADS.
- Thernisien, A.: 2011, Implementation of the graduated cylindrical shell model for the three-dimensional reconstruction of coronal mass ejections. *Astrophys. J. Suppl.* **194**, 33. DOI ADS.
- Thernisien, A., Vourlidas, A., Howard, R.A.: 2009, Forward modeling of coronal mass ejections using STEREO/SECCHI data. *Solar Phys.* **256**, 111. DOI ADS.
- Thernisien, A., Vourlidas, A., Howard, R.A.: 2011, CME reconstruction: pre-STEREO and STEREO era. *J. Atmos. Solar-Terr. Phys.* **73**, 1156. DOI ADS.
- Thompson, W.T.: 2006, Coordinate systems for solar image data. *Astron. Astrophys.* **449**, 791. DOI ADS.
- Thompson, W.T.: 2009, 3D triangulation of a Sun-grazing comet. *Icarus* **200**, 351. DOI ADS.
- Thompson, W.T., Reginald, N.L.: 2008, The radiometric and pointing calibration of SECCHI COR1 on STEREO. *Solar Phys.* **250**, 443. DOI ADS.
- Vourlidas, A., Howard, R.A., Plunkett, S.P., Korendyke, C.M., Thernisien, A.F.R., Wang, D., Rich, N., Carter, M.T., Chua, D.H., Socker, D.G., Linton, M.G., Morrill, J.S., Lynch, S., Thurn, A., Van Duyne, P., Haggood, R., Clifford, G., Grey, P.J., Velli, M., Liewer, P.C., Hall, J.R., DeJong, E.M., Mikic, Z., Rochus, P., Mazy, E., Bothmer, V., Rodmann, J.: 2016, The Wide-Field Imager for Solar Probe Plus (WISPR). *Space Sci. Rev.* **204**, 83. DOI ADS.
- Wang, Y.-M., Sheeley, J.N.R.: 1992, On potential field models of the Solar Corona. *Astrophys. J.* **392**, 310. DOI ADS.
- Webb, D.F., Howard, T.A.: 2012, Coronal mass ejections: observations. *Living Rev. Solar Phys.* **9**, 3. DOI.
- Wheatland, M.S., Sturrock, P.A., Roumeliotis, G.: 2000, An optimization approach to reconstructing force-free fields. *Astrophys. J.* **540**, 1150.
- Wiegelmann, T.: 2004, Optimization code with weighting function for the reconstruction of coronal magnetic fields. *Solar Phys.* **219**, 87.
- Wiegelmann, T., Inhester, B.: 2010, How to deal with measurement errors and lacking data in nonlinear force-free coronal magnetic field modelling? *Astron. Astrophys.* **516**, A107.
- Wiegelmann, T., Sakurai, T.: 2012, Solar force-free magnetic fields. *Living Rev. Solar Phys.* **9**, 5. DOI.
- Xie, H., St. Cyr, O.C., Gopalswamy, N., Yashiro, S., Krall, J., Kramar, M., Davila, J.: 2009, On the origin, 3D structure and dynamic evolution of CMEs near solar minimum. *Solar Phys.* **259**, 143. DOI ADS.

- Yang, J., Dai, J., Chen, H., Li, H., Jiang, Y.: 2018, Filament eruption with a deflection of nearly 90 degrees. *Astrophys. J.* **862**, 86. DOI. ADS.
- Yashiro, S., Gopalswamy, N., Michalek, G., St. Cyr, O.C., Plunkett, S.P., Rich, N.B., Howard, R.A.: 2004, A catalog of white light coronal mass ejections observed by the SOHO spacecraft. *J. Geophys. Res.* **109**, A07105. DOI. ADS.

Publisher's Note Springer Nature remains neutral with regard to jurisdictional claims in published maps and institutional affiliations.

Authors and Affiliations

Marilena Mierla^{1,2} · Hebe Cremades³ · Vincenzo Andretta⁴ · Iulia Chifu⁵ · Andrei N. Zhukov^{1,6} · Roberto Susino⁷ · Frédéric Auchère⁸ · Angelos Vourlidas⁹ · Dana-Camelia Talpeanu¹ · Luciano Rodriguez¹ · Jan Janssens¹ · Bogdan Nicula¹ · Regina Aznar Cuadrado¹⁰ · David Berghmans¹ · Alessandro Bemporad⁷ · Elke D'Huys¹ · Laurent Dolla¹ · Samuel Gissot¹ · Giovanna Jerse¹¹ · Emil Kraaikamp¹ · David M. Long^{12,13} · Benjamin Mampaey¹ · Christian Möstl¹⁴ · Paolo Pagano^{15,16} · Susanna Parenti⁸ · Matthew J. West¹⁷ · Olena Podladchikova^{18,19} · Marco Romoli^{20,21} · Clementina Sasso⁴ · Koen Stegen¹ · Luca Teriaca¹⁰ · William Thompson²² · Cis Verbeek¹ · Emma Davies²³

✉ R. Aznar Cuadrado
aznar@mps.mpg.de

- ¹ Solar-Terrestrial Centre of Excellence - SIDC, Royal Observatory of Belgium, Avenue Circulaire 3, Brussels 1180, Belgium
- ² Institute of Geodynamics of the Romanian Academy, Bucharest, Romania
- ³ Grupo de Estudios en Heliofísica de Mendoza, CONICET, Universidad de Mendoza, 665 Boulogne Sur Mer, Mendoza 5500, Argentina
- ⁴ INAF - Istituto Nazionale di Astrofisica, Osservatorio Astronomico di Capodimonte, Salita Moiariello 16, I-80131 Napoli, Italy
- ⁵ Institut fuer Astrophysik, University of Goettingen, Germany, Friedrich-Hund-Platz 1, 37077 Goettingen, Germany
- ⁶ Skobel'syn Institute of Nuclear Physics, Moscow State University, 119992 Moscow, Russia
- ⁷ INAF - Istituto Nazionale di Astrofisica, Osservatorio Astrofisico di Torino, Via Osservatorio 20, Pino T.se, Torino, Italy
- ⁸ Université Paris-Saclay, CNRS, Institut d'Astrophysique Spatiale, 91405, Orsay, France
- ⁹ Johns Hopkins University Applied Physics Laboratory, Laurel, MD, US
- ¹⁰ Max-Planck-Institut für Sonnensystemforschung, Justus-von-Liebig-Weg 3, 37077 Goettingen, Germany
- ¹¹ INAF OATS (National Institute of Astrophysics - Observatory of Trieste), Trieste, Italy
- ¹² Mullard Space Science Laboratory, University College London, Holmbury St. Mary, Dorking, Surrey, RH5 6NT, UK
- ¹³ Astrophysics Research Centre, School of Mathematics and Physics, Queen's University Belfast, University Road, Belfast, BT7 1NN, Northern Ireland, UK
- ¹⁴ Austrian Space Weather Office, GeoSphere Austria, Reininghausstrasse 3, 8020 Graz, Austria

- 15 Dipartimento di Fisica e Chimica, Università di Palermo, Piazza del Parlamento 1, I-90134 Palermo, Italy
- 16 INAF-Osservatorio Astronomico di Palermo, Piazza del Parlamento 1, I-90134 Palermo, Italy
- 17 Southwest Research Institute, 1050 Walnut Street, Suite 300, Boulder, CO 80302, USA
- 18 Leibniz Institute for Astrophysics Potsdam, An der Sternwarte 16, 14482 Potsdam, Germany
- 19 National Polytechnic University of Ukraine, 37, 03056, Prosp. Peremohy, Kyiv, Ukraine
- 20 Dipartimento di Fisica e Astronomia, Università di Firenze, I-50019 Sesto Fiorentino FI, Italy
- 21 INAF — Associate Scientist, Rome, Italy
- 22 Adnet Systems Inc., NASA Goddard Space Flight Center, Code 671, Greenbelt, MD 20771, USA
- 23 Institute for the Study of Earth, Ocean, and Space, University of New Hampshire, Durham, NH, USA